OCT 1999

REPORT DOCUMENTATION PAGE

AFRL-SR-BL-TR-99-

0248

1. AGENCY USE ONLY (Leave blank)	2. REPORT DATE	3. REPORT TYPE AND DATES COVERED
	9/25/99	Final Technical Report 7/1/96-6/30/99

4. TITLE AND SUBTITLE

(U) Computational Investigation of Atomization

5. FUNDING NUMBERS

PE-61102F
PR-2308
SA-BX

G – F49620-96-1-0356

6. AUTHOR(S)

Gretar Tryggvason

7. PERFORMING ORGANIZATION NAME(S) AND ADDRESS(ES)

University of Michigan
Dept. of Mechanical Engineering
2031 Lay Automotive Lab.
Ann Arbor, MI 48109-2121

8. PERFORMING ORGANIZATION REPORT NUMBER

9. SPONSORING / MONITORING AGENCY NAME(S) AND ADDRESS(ES)

AFOSR/NA
801 North Randolph Street
Room 732
Arlington, VA 22203-1977

10. SPONSORING / MONITORING AGENCY REPORT NUMBER

11. SUPPLEMENTARY NOTES

12a. DISTRIBUTION / AVAILABILITY STATEMENT

Approved for public release; distribution is unlimited

12b. DISTRIBUTION CODE

13. ABSTRACT *(Maximum 200 Words)*

The secondary breakup of liquid fuel drops was studied by numerical simulations. The Navier-Stokes equations were solved by a finite difference/front tracking technique that included inertia, viscous forces, and surface tension at the deformable boundary between the fuel and the air. The breakup of drops accelerated impulsively as well as by a constant body force was studied by axisymmetric simulations for two different density ratios (1.15 and 10). The low density ratio results can be used for other density ratios by simple rescaling of time. It was shown that the drops break up in different modes, depending on the relative strength of surface tension versus inertia. The modes are similar to those found experimentally for drops in air at atmospheric pressure and breakup maps constructed from the computational results show similar transitions. There are, however, some differences. Bag breakup is, for example, not found for impulsively accelerated drops in the low density ration limit. Computations of the heat transfer of drops that are breaking up shows a rapid increase, and the drops often reach the ambient temperature before breakup is completed. Three-dimensional simulations show that while drops undergoing breakup remain axisymmetric initially, eventually they are unstable to three-dimensional disturbances.

14. SUBJECT TERMS

Atomization, Spray, Secondary breakup of drops

15. NUMBER OF PAGES

83

16. PRICE CODE

17. SECURITY CLASSIFICATION OF REPORT	18. SECURITY CLASSIFICATION OF THIS PAGE	19. SECURITY CLASSIFICATION OF ABSTRACT	20. LIMITATION OF ABSTRACT
Unclassified	Unclassified	Unclassified	UL

Contents

EXECUTIVE SUMMARY

Numerical simulations of the deformations and breakup of drops have been done. Inertial and viscous effects for both the drop and the ambient gas as well as surface tension effects are fully accounted for. The simulations help determine where in parameter space the various breakup modes take place, how long breakup takes, and what the resulting drop size distribution is. The goal of the investigation is to provide results that extend and complement experimental investigations, and lead to better engineering models of drops in sprays. Simulations of the primary breakup of a flat interface have also been done.

To examine the breakup of drops as the density difference becomes small, extensive axisymmetric simulation of four systems have been done: Impulsive and gradual disturbances for two different density ratios. At low density ratios, the density disappears as an independent control parameter and it can be shown that the low density results apply to density ratios as high as two if time is re-scaled using the Boussinesq approximation. In addition to full simulations where the Navier-Stokes equations are solved, a few inviscid simulations have also been done to isolate the effect of viscosity.

Four nondimensional numbers govern the breakup of drops. In addition to the density and the viscosity ratio, the ratio of inertia to surface tension is described by an Eötvös number for gradual disturbances and a Weber number for impulsive acceleration. The effect of viscosity is described by the Ohnesorge number (the ratio of the viscous force to the surface tension). The simulations have resulted in a fairly complete picture of the evolution at small density ratios. For small Eötvös and Weber numbers the drops remain spherical in all cases, independent of the Ohnesorge number and the density and the viscosity ratio. If the Ohnesorge number is low, the deformations of the drop depend only on the Eötvös/Weber number (and the density ratio). As the Eötvös/Weber number is increased, the drops deform into a disk-like shape due to high pressure at the fore and aft stagnation points and low pressure around the equator. Increasing the Eötvös/Weber number further results in a continuing deformation where most of the drop fluid ends up in a torus connected by a thin film. For moderate Eötvös/Weber numbers, the initial

momentum of the drops is relatively low and once the torus is formed, the rim moves faster than the film for drops with gradual disturbances. The film "bulges" back and experimentally it is seen that this bag eventually breaks. The simulations have shown that the bag break-up mode is a viscous phenomenon, due to flow separation at the rim of the drops and the formation of a wake, and it is therefore not seen in inviscid computation. For drops subject to an impulsive acceleration, the formation of a backward facing bag is only seen for the higher density ratios. Bag breakup requires a driving force that acts stronger on the drop than on the surrounding fluid and for impulsively accelerated drops this driving force is the fluid inertia. As the density difference becomes small, the difference between the drop and the fluid inertia vanishes and the low-density ratio drops simply stop and surface tension pulls them back into a spherical shape. Experimentally, bag breakup is commonly observed for impulsive acceleration, but the density ratio is much larger. Increasing the Eötvös or the Weber further results in a different mode of breakup that also depends on the density ratio. For low density ratios, the fluid initially still ends up in the rim of the drop, but the initial momentum is now sufficiently large so the ambient fluid moves the film faster than the torus, leading to a bag that extends forward of the drop. For higher density ratios, not all the fluid moves to the rim and a torus that is connected to the rest of the drop by a thin sheet is formed. As the driving force is increased the size of the rim is reduced and for very high Eötvös/Weber numbers, small drops are pulled from the rim. Examination of the dynamic of the vorticity generated at the drop suggests that the shear breakup mode where fluid is stripped from the rim of the drop is an essentially inviscid effect. In the transition between a bag breakup mode and shear breakup, drops that oscillate in a chaotic manner are sometimes seen. Such transition phenomena have been seen experimentally for higher density ratios. In addition to the Ohnesorge number effect, where the boundary between breakup modes is shifted to higher Eötvös/Weber numbers as viscous effects become more important, the fluid and drop viscosity can change the drop shape during breakup if the Ohnesorge number is high enough. High viscosities can, for example lead to skirted drops at low density ratios, where thin fluid skirts are pulled from the rim of the fluid, in a way similar to the shear breakup seen for higher density ratios.

The simulations have been used to generate "break-up" maps and it is found that the general

character of those maps agrees with what has been found experimentally for larger density ratios. At low Ohnesorge numbers the transition between the various modes depends only on the density ratio and the Eötvös number, but a high Ohnesorge number will move the transition to a higher Eötvös number.

Simulations of three-dimensional aspects of the drop breakup and heat transfer have recently been initiated.

PERSONNEL SUPPORTED:

Salih Ozen Unverdi, Research Fellow

Jaehoon Han, Graduate Student and Research Fellow

PUBLICATIONS

J. Han and G. Tryggvason. Secondary Breakup of Liquid Drops in Axisymmetric Geometry-Part I, Acceleration by a Constant Body Force. Phys. Fluids Dec. 1999.

G. Tryggvason and S.O. Unverdi. The Shear Breakup of an Immiscible Fluid Interface. Fluid Dynamics at Interfaces" (Ed. W. Shyy) Cambridge University Press, 1999. The book was just published, the full citation with page numbers will be available shortly.

G. Tryggvason, B. Bunner, O. Ebrat, and W. Tauber. Computations of Multiphase Flows by a Finite Difference/Front Tracking Method. I Multi-Fluid Flows. In: 29th Computational Fluid Dynamics. Lecture Series 1998-03. Von Karman Institute for Fluid Dynamics.

G. Tryggvason, A. Esmaeeli, S. Mortazavi, J. Han, and S. Homma. Computations of Multiphase Flows by a Finite Difference/Front Tracking Method. II Applications. In: 29th Computational Fluid Dynamics. Lecture Series 1998-03. Von Karman Institute for Fluid Dynamics

J. Han: *Numerical Studies of Drop Motion in Axisymmetric Geometry*. Ph. D. Dissertation. The University of Michigan, 1998.

W. Tauber, S.O. Unverdi, and G. Tryggvason. Formation of Drops by Interfacial Shear. FEDSM98-5217. Proceedings of the 1998 ASME Fluids Engineering Division Summer Meeting, Washington, D.C., June 21-25, 1998.

W. Tauber and G. Tryggvason The Shear Breakup of Immiscible Round Jets Proceedings of the 1999 ASME Fluids Engineering Division Summer Meeting, San Francisco, CA July 18-22, 1999.

J. Han and G. Tryggvason. Secondary Breakup of drops. Proceedings of the 1999 ASME Fluids Engineering Division Summer Meeting, San Francisco, CA July 18-22, 1999.

PRESENTATIONS

J. Han & G. Tryggvason, "A Numerical Study of the Secondary Breakup of Liquid Drops. 49th Meeting of the American Physical Society, Div. of Fluid Dynamics, Abstracts in Bull. Amer. Phys. Soc. 41: 1721, Syracuse, NY, Nov. 24-26, 1996.

G. Tryggvason. "Direct Numerical Simulations of Multiphase Flows." Institute for Multiphase Flow Science and Technology. Feb 28-March 1, 1997

J. Han and G. Tryggvason: 50th Meeting of the American Physical Society, Div of Fluid Dynamics, Abstracts in Bull. Amer. Phys. Soc. Nov, 1997 G. Tryggvason, B. Bunner, S. Mortazavi, & A. Esmaeeli "Direct Numerical Simulations of Dispersed Multiphase Flows," Proceedings of of the 11 Japanese Symposium on CFD. Tokyo, Japan. December, 1997. Invited Opening Lecture.

W. Tauber, S.O. Unverdi, and G. Tryggvason. The Shear Breakup of an immiscible fluid interface. 51th Meeting of the American Physical Society, Div of Fluid Dynamics, Abstracts in Bull. Amer. Phys. Soc. 43: 2030, Philadelphia, PA, Nov. 22-24, 1998.

J. Han and G. Tryggvason. Secondary Breakup of Liquid Drops in Axisymmetric Geometry. 51th Meeting of the American Physical Society, Div of Fluid Dynamics, Abstracts in Bull. Amer. Phys. Soc. 43: 2044, Philadelphia, PA, Nov. 22-24, 1998.

W. Tauber, S.O. Unverdi, and G. Tryggvason. The Shear Breakup of an immiscible fluid interface. 51th Meeting of the American Physical Society, Div of Fluid Dynamics, Abstracts in Bull. Amer. Phys. Soc. 43: 2030, Philadelphia, PA, Nov. 22-24, 1998.

G. Tryggvason. Seminar at Rutgers University, 2/12/99

G. Tryggvason. Lectures as part of a "Short Course on Modeling and Computation of Multiphase Flow, Part IIB: Multiphase flow CFD", March 8-12, 1999. Zurich, Switzerland

G. Tryggvason. Direct Numerical Simulations of Multiphase Flow. American Physical Society Centennial Meeting, Atlanta, GA. March 20-26, 1999. Invited talk in a special session organized by the computational physics division of APS at the APS Centennial meeting in Atlanta.

G. Tryggvason. Direct Numerical Simulations of Dispersed Flow. 9th Workshop on Two-Phase Flow Predictions, Merseburg , Germany, April 13-16, 1999

G. Tryggvason. Co-organizer and co-principal lectures in a short course: Suivis d'interfaces, INRIA Rocquencourt, France, May 3-6, 1999.

G. Tryggvason. Invited presentation on Direct Numerical Simulations of Atomization. 12th Annual Conference on Liquid Atomization and Spray Systems, Indianapolis, IN, May 16-19, 1999

G. Tryggvason. Direct simulations of disperse flows. ICIAM 99, Edinburg, Scotland, July 5-9, 1999

G. Tryggvason. Direct simulations of multiphase flows. Invited talk. Interfaces for the 21 century. Monterey, CA. August 16-18

W. Tauber and G. Tryggvason. A presentation at the 8th International Symposium on CFD (ISCFD). September 5-10,1999, Bremen, Germany.

I. BACKGROUND

In spray combustion, liquid atomization is a two stage process: In the primary breakup, a liquid jet emerging from the injector breaks up into drops which subsequently undergo secondary breakup into even smaller drops. Secondary breakup increases the total surface area of the fuel-air interface, thus enhancing the rate at which the fuel evaporates and burns.

Current computational models used for engineering predictions of spray combustion do not resolve the motion of individual drops. Instead, the effect of the drops is accounted for by subgrid models, computed in either an Eulerian or a Lagrangian way. For recent descriptions and reviews, see Drew and Passman[1] and Crowe, Sommerfeld, and Tsuji[2]. In Lagrangian models, the drops are represented by point particles, that can be split into two or more particles to represent drop breakup. For a description and application of breakup models in spray combustion simulations, see Reitz and Diwakar[3], O'Rourke and Amsden[4], Liu, Mather, and Reitz[5], Liu and Reitz[6], Kim and Wang[7], and Kong, Han, and Reitz[8]. Two different approaches are typically used to model the breakup. The Taylor analogy breakup (TAB) model of O'Rourke and Amsden[4] is based on an analogy between an oscillating and distorting liquid drop and a spring-mass system suggested by Taylor[9]. The Reitz wave instability model[6], on the other hand, is based on a linear stability analysis for liquid jets. Both of these simplified models contain adjustable parameters that must be determined by experimental studies.

In experiments, the drops are usually accelerated by a shock wave causing a step change in the velocity of the drop relative to the surrounding fluid, or by a constant body force such as gravity. The results are generally presented in terms of four non-dimensional parameters: the relative strength of inertia and surface tension which is characterized by the Weber number for an impulsive acceleration and the Eötvös number for an acceleration by a constant body force; the ratio of viscous stresses and surface tension given by the Ohnesorge number; the density ratio; and the viscosity ratio of the drop and surrounding fluids.

Early experimental studies of drop breakup due to impulsive acceleration include those of Lane[10], who studied the shattering of liquid drops in steady or transient streams of air, and Hinze[11].

The findings of Lane[10] and Hinze[11] have been extended to a broader range of parameters by Haas[12], Hanson, Domich, and Adams[13], Ranger and Nicholls[14], Gel'fand, Gubin, Kogarko, and Komar[15], Borisov, Gel'fand, Natanzon, and Kossov[16], and others. Krzeczkowski[17] showed that the effect of drop viscosity is not significant when the Ohnesorge number based on the drop properties is less than about 0.1. Pilch and Erdman[18] examined the fragment size distribution for the so-called bag breakup mode and found that it was made up of a large number of small fragments produced from the burst of the bag, and a few large fragments originating from the annular rim. Wierzba[19] reviewed the literature and found that there was a large variation in the reported values of the critical Weber numbers for the onset of the bag type breakup. His own experiments showed that small changes in the experimental conditions could affect the drop breakup significantly. Experimental investigations of the breakup of falling drops have typically been motivated by interest in the evolution of raindrops. For early experiments, see the study of the breakup of large drops by Magarvey and Taylor[20], for example. The secondary breakup of liquid drops due to both impulsive and continuous disturbances has been examined extensively by Hsiang and Faeth[21–23] using a shock tube and drop towers. The majority of the data are for atmospheric conditions ($\rho_d/\rho_o > 500$, $Re > 100$, $Oh_d < 0.1$), although a limited number of studies for smaller density ratios and higher viscosity were also done. For the impulsive disturbance case, droplet deformation and breakup maps similar to those produced by Hinze[11] and Krzeczkowski[17] were constructed for a wide range of parameters. Joseph, Belanger, and Beavers[24] studied the breakup of both Newtonian and non-Newtonian drops in a high-speed air stream. Their experiments, using a shock tube, resulted in a very high initial acceleration of drops and the authors stated that the Rayleigh-Taylor instability was the primary cause of breakup. For a more extensive review of experimental studies of secondary breakup of drops, see Clift, Grace and Weber[25], Lefebvre[26], Bayvel and Orzechowski[27], and Sadhal, Ayyaswamy, and Chung[28].

Most of the experimental studies mentioned previously are concerned with the breakup of liquid drops in air due to impulsive accelerations. The density and viscosity ratios are much higher than those considered in the present study. While those experimental results are not directly comparable to our simulations, the major breakup modes remain similar. We therefore summarize the

major results of experimental studies of impulsively accelerated drops here. When the Ohnesorge number is small, the effects of drop viscosity can be neglected. At low We, the drops deform but do not break up. As the acceleration increases past a critical value, the drops become progressively flatter and eventually break up. As the Weber number is increased, four well defined breakup modes are observed (see, for example, Nigmatulin[29]):

1. Vibrational breakup mode where the drop disintegrates into two or four equal-sized smaller drops.

2. Bag breakup mode where the original drop deforms into a torus-shaped rim spanned by a thin fluid film that ruptures into tiny droplets, followed by disintegration of the rim into larger droplets.

3. Shear breakup mode where small drops are continuously stripped off the rim of the original drop.

4. Explosive breakup mode where strong surface waves disintegrate the drop in a violent manner.

This categorization and terminology are somewhat arbitrary, and other variations have been suggested by other researchers. For example, mode 3 has also been called "stripping-type breakup."[18,19] For low viscosity drops where the transition process shows no significant dependencies on Oh_d, the critical Weber number is approximately 10 for the first transition, 20–60 for the second, and 1000 for the third. These numbers should be considered only as a rough guide because there are large variations in the critical Weber numbers in the available experimental data due to different test conditions. At higher Oh_d, the We required for the onset of deformation and breakup increases with increasing Oh_d.

Other researchers have examined the evolution of liquid drops in another liquid with a density comparable to the drop density moving due to gravity. The deformation of miscible liquid drops at low Reynolds numbers was studied by Kojima, Hinch, and Acrivos[30], who observed that the drops form vortex rings. The stability of drops moving in immiscible fluids was investigated by

Koh and Leal[31,32], who showed computational results for zero Reynolds number using a boundary integral method and experimental results for low Reynolds numbers. A similar investigation of the instability of drops, also using a boundary integral method was reported by Pozrikidis[33]. Experiments by Baumann, Joseph, Mohr, and Renardy[34] showed that vortex rings can also be created in immiscible liquids.

A few investigators have simulated the deformation and breakup of liquid drops numerically. However, due to the difficulties in dealing with large deformation of the interface and in accurately including surface tension along with viscous and inertial forces, such numerical simulations have often been based on considerable simplifications. The steady motion of deformable axisymmetric drops was investigated by Dandy and Leal[35] at several Reynolds and Weber numbers using a finite-difference method. The steady rise of an axisymmetric drop in an unbounded surrounding fluid was examined by Volkov[36] for intermediate Reynolds numbers. Bozzi, Feng, Scott, and Pearlstein[37] presented finite element simulations of the steady motion of axisymmetric drops in bounded domains. Fritts, Fyre, and Oran[38] applied a two-dimensional Lagrangian finite difference method to simulate the breakup of fuel droplets and Liang, Eastes, and Gharakhari[39] presented simulations of axisymmetric drop breakup using a Volume-of-Fluid method for a limited number of cases. Other numerical studies of the deformation and breakup of two-dimensional drops can be found in Deng and Jeng[40], Deng, Liaw, and Chou[41], Seung, Chen, and Chen[42], and Zaleski, Li, and Succi[43]. However, these numerical results are still preliminary.

In spite of the progress made by previous investigators, several aspects of the secondary breakup are still not well understood, including the breakup of drops at high pressure and temperature, where experimental difficulties are encountered. It is also necessary to more closely examine the time dependent characteristics of the breakup. In existing spray models, the drop breakup is considered to occur instantaneously. Recent experimental evidence indicates, however, that secondary breakup occurs over a finite amount of time. Therefore, it is possible that the drop breakup should be treated as a time-dependent process.

In this paper, a numerical method based on a front tracking technique that can accommodate large deformation of the drops is developed to simulate the breakup of liquid drops accelerated by a

constant body force. The governing equations for axisymmetric geometry are solved numerically on a non-uniform grid using a finite difference method. The drop interface is represented by connected marker points, whose positions are updated explicitly at each time-step. Results for a wide range of parameters are presented, and the physical significance of the results is discussed.

II. FORMULATION AND NUMERICAL METHOD

The physical problem and computational domain are sketched in Figure 1; the left boundary is the axis of symmetry. We follow the motion of the fluids both inside and outside the drop and write a single set of equations for the whole flow field, using the conservative form of the governing equations to allow the density and viscosity to change discontinuously. Surface tension is added as a delta function to provide the proper interface boundary conditions. Written for an axisymmetric coordinate system, the Navier-Stokes equations are:

$$\frac{\partial \rho u}{\partial t} + \frac{1}{r}\frac{\partial r \rho u^2}{\partial r} + \frac{\partial \rho v u}{\partial z} = -\frac{\partial p}{\partial r} + \frac{\partial}{\partial r}\left(2\mu \frac{\partial u}{\partial r}\right) + 2\mu \frac{\partial}{\partial r}\left(\frac{u}{r}\right) + \frac{\partial}{\partial z}\mu\left(\frac{\partial v}{\partial r} + \frac{\partial u}{\partial z}\right) - \int_S \sigma \kappa \vec{n} \delta(\vec{x} - \vec{x}_f) dS \cdot \hat{i}_r \tag{1}$$

$$\frac{\partial \rho v}{\partial t} + \frac{1}{r}\frac{\partial r \rho u v}{\partial r} + \frac{\partial \rho v^2}{\partial z} = -\frac{\partial p}{\partial z} + \frac{1}{r}\frac{\partial}{\partial r}\mu r\left(\frac{\partial v}{\partial r} + \frac{\partial u}{\partial z}\right) + \frac{\partial}{\partial z}\left(2\mu \frac{\partial v}{\partial z}\right) - \int_S \sigma \kappa \vec{n} \delta(\vec{x} - \vec{x}_f) dS \cdot \hat{i}_z - \rho a_z \tag{2}$$

Here, u and v are the velocity components in the radial and axial directions, p is the pressure, and ρ and μ are the discontinuous density and viscosity fields, σ is the surface tension, κ is twice the mean curvature, $\hat{i}_r$ and $\hat{i}_z$ are the radial and axial components of the surface unit normal vector pointing outward from the drop, and δ is a three-dimensional delta function. In (1) and (2), the surface tension is treated as a body force. The integral over the surface of the drop, S, results in a force that is smooth and continuous along the drop surface. In the numerical method, the delta

function, δ, is approximated by a smooth function with a compact but finite support. The constant acceleration gives rise to a body force in the axial direction denoted by ρa_z.

The above equations are supplemented by the incompressibility condition:

$$\frac{1}{r}\frac{\partial ru}{\partial r} + \frac{\partial v}{\partial z} = 0 \tag{3}$$

which, when combined with the momentum equations, leads to an elliptic equation for the pressure:

$$\nabla \cdot \left(\frac{\nabla p}{\rho}\right) = \frac{1}{\rho} R \tag{4}$$

where R is the divergence of the vector form of the momentum equations (1) and (2), excluding the pressure term.

We also have equations of state for the physical properties of the drop and the surrounding fluid:

$$\frac{D\rho}{Dt} = 0\,;\ \frac{D\mu}{Dt} = 0 \tag{5}$$

where D/Dt is the material derivative. These two equations state that the physical properties of each fluid remain constant.

Dimensional analysis shows that four independent dimensionless parameters govern the dynamics of drop deformation and breakup. When the drop is subject to an acceleration by a constant body force, it is convenient to use the Eötvös number, Eo (interchangeably called the Bond number, Bo) and the Ohnesorge number of the drop, Oh_d, defined as:

$$Eo = \frac{a_z \Delta\rho D^2}{\sigma} \tag{6}$$

$$Oh_d = \frac{\mu_d}{\sqrt{\rho_d D \sigma}} \tag{7}$$

where $\Delta\rho$ is the density difference between the drop and the surrounding fluid and D is the initial diameter of the drop. The density and the viscosity ratios:

$$\frac{\rho_d}{\rho_o}\,;\ \frac{\mu_d}{\mu_o} \tag{8}$$

can be selected as the other two parameters. The viscosity ratio is sometimes replaced by the Ohnesorge number based on the properties of the surrounding fluid:

$$Oh_o = \frac{\mu_o}{\sqrt{\rho_o D \sigma}} \tag{9}$$

The subscripts, d and o, denote the properties of the drop and the surrounding fluid, respectively. Time is non-dimensionalized with respect to the drop diameter and the acceleration:

$$t^* = \frac{t}{\sqrt{D/a_z}} \tag{10}$$

For drops subject to impulsive acceleration, the Weber number, We defined by:

$$We = \frac{\rho_o U^2 D}{\sigma} \tag{11}$$

is used in place of the Eötvös number and the Ohnesorge number is often replaced by the Reynolds number defined by:

$$Re = \frac{\rho_o U D}{\mu_o} \tag{12}$$

Here, U is the initial relative velocity between the drop and the surrounding fluid. Time is non-dimensionalized with the diameter and the initial relative velocity:

$$t^* = \frac{t}{(D/U)} \tag{13}$$

The numerical technique used for the simulations presented here is based on the front-tracking/finite difference method discussed in Unverdi and Tryggvason[44]. The code employed in the present study is an axisymmetric version of the method. Since the axisymmetric code runs much faster than the fully three-dimensional version, it allows more runs and higher resolution. To improve the efficiency of the computations, the method was implemented on stretched grids to allow clustering of grid points in specific regions.

The momentum equations and the continuity equation are discretized using an explicit second-order predictor-corrector time-integration method and a second-order centered difference approximation for the spatial derivatives. The discretized equations are solved on a fixed, staggered grid

using the Marker-and-Cell method developed by Harlow and Welch[45]. The full-slip boundary condition is applied to all four boundaries.

To maintain a well defined boundary between the drops and the surrounding fluid, the boundary is marked by connected points (the front) that are advected by the fluid velocity, interpolated from the fixed grid. The new position of the marker points is used to construct a new density field by distributing the density jump to the grid points next to the front using area weighting, and integrating the jump to find the density everywhere. Once the density is known, the viscosity is set as a function of the density. The marker points are also used to find the surface tension, which is then assigned to the nearest grid points in the same way as the density jump, and added to the discrete Navier-Stokes equations. For a more detailed description of the front tracking method, see Unverdi and Tryggvason[44] and Tryggvason, Bunner, Ebrat, and Tauber[46].

The implementation of the numerical technique to the drop breakup problem is straightforward and the method works well for a broad range of parameters. However, as ρ_d/ρ_o is raised, the computational cost increases, partly because of the appearance of the coefficient $1/\rho$ in the pressure equation (4) but also because the effect of the surrounding fluid is weaker when the density ratio is large and the drop travels a longer distance before breaking up. In order to avoid having to use a very long computational domain, we move the computational domain with the drop. The motion of the domain is determined from the solution, and an extra acceleration term is added to the governing equations to account for the time dependent motion of the domain. The boundary conditions have also been modified to include a constant inflow at the bottom and a zero velocity gradient in the normal direction at the top.

The majority of the simulations presented here were carried out on HP 9000 workstations. A typical run required between 4000 and 120000 timesteps and took 12–240 hours, depending on the parameters of the problem.

To address to what extend the observed drop evolution can be described by an inviscid model, a few simulations were done using a vortex method. The interface separating the drop and the surrounding fluid is a vortex sheet and an evolution equation for the vortex sheet strength $\gamma = (\mathbf{u}_d - \mathbf{u}_o) \cdot \mathbf{s}$ can be derived by subtracting the tangential components of the Euler's equations on

either side of the interface. The resulting equation is (see, for example, Tryggvason[47]):

$$\frac{D\gamma}{Dt} + \gamma \frac{\partial \mathbf{U}}{\partial s} \cdot \mathbf{s} = 2A\Big(\frac{d\mathbf{U}}{dt} \cdot \mathbf{s} + \frac{1}{8}\frac{\partial \gamma^2}{\partial s}\Big) - \frac{\sigma}{\rho_d + \rho_o}\frac{\partial \kappa}{\partial s} \tag{14}$$

Here, $A = (\rho_d + \rho_o)/\rho_d + \rho_o$ is the Atwood number, $\mathbf{U} = (1/2)(\mathbf{u}_d + \mathbf{u}_o)$ is the average of the velocities on either side of the vortex sheet, and κ is the mean curvature.

Given the vortex sheet strength γ, the velocity is found by the Biot-Savart integral. For computational purpose, the axisymmetric vortex sheet is discretized by a finite number of vortex rings. The azimuthal integration can be done analytically and the integral is therefore replaced by a summation over the discrete vortex rings. The radial and axial velocity at point on ring j is given by

$$v_j = \frac{1}{\pi}\sum_{l=1}^{N} \frac{\Gamma_l\, r_l\, k_{lj}(z_j - z_l)}{(4 r_j\, r_l)^{3/2}}\Big[\Big(\frac{k_{lj}^2 - 2}{1 - k_{lj}^2}\Big)E(k_{lj}) + 2K(k_{lj})\Big] \tag{15}$$

$$u_j = \frac{1}{\pi}\sum_{l=1}^{N} \frac{\Gamma_l\, r_l\, k_{lj}}{(4 r_j\, r_l)^{3/2}}\Big[\Big(\frac{(r_l + r_j)k_{lj}^2 - 2r_l}{1 - k_{lj}^2}\Big)E(k_{lj}) + 2r_l K(k_{lj})\Big] \tag{16}$$

Here $K(k)$ is the Complete Elliptic integral of the first kind, $E(k)$ is the Complete Elliptic integral of the second kind, and

$$k_{lj} = \frac{2\sqrt{r_l\, r_j}}{\sqrt{(r_l + r_j)^2 + (z_j - z_l)^2}} \tag{17}$$

The Elliptic integrals can be computed efficiently by a polynomial approximation. When the axisymmetric vortex sheet is replaced by discrete vortex rings, the rings must be given a finite core size to avoid infinite self-induced velocity. This can be accomplished simply by replacing k_{lj} by

$$\tilde{k}_{lj} = \frac{2\sqrt{r_l\, r_j}}{\sqrt{(r_l + r_j)^2 + (z_j - z_l)^2 + \delta^2}} \tag{18}$$

where δ is a small regularization parameter. In the limit of $N \to \infty$ and $\delta \to 0$ the solution will be independent of the exact value of δ (except at isolated points where roll-up takes place).

III. ACCELERATION BY A CONSTANT BODY FORCE

Numerical simulations are presented first for $\rho_d/\rho_o = 10$, using a moving computational domain. To examine the effect of the density ratio, simulations are also carried out for a small density

ratio, $\rho_d/\rho_o = 1.15$, using a fixed computational domain. For each density ratio, the effects of varying the other dimensionless parameters, Eo, Oh_o, and Oh_d, are studied.

A. Validation

In order to validate the numerical method, grid refinement tests were performed. Typical results are presented in Figure 2 where the shape of the drop is plotted at time intervals $\Delta t_p^* = 3.873$, using two different grids: 256×512 (left) and 512×1024 (right). The non-dimensional parameters are $\rho_d/\rho_o = 1.15$, $Eo = 144$, $Oh_o = 0.05$, and $Oh_d = 0.0466$. Initially ($t^* = 0$), the drops are spherical and the velocities are zero everywhere. Despite the large deformation of the drop, the results agree well. In Figure 3, the aspect ratio and the centroid velocity are plotted versus non-dimensional time. The aspect ratio is defined as the maximum width of the drop divided by its thickness at the centerline. The centroid velocity is found by taking the volume average of the vertical velocity inside the drop. The results corresponding to Figure 2 are shown along with results using a coarser grid: 128×256. The result from the 128×256 grid shows a small difference but the two finer grids give nearly identical results.

In addition, we have compared our results to the steady state results for a single axisymmetric deformable drop computed by Dandy and Leal[35]. They specified the Reynolds number and the Weber number and found the drag coefficient, C_d, as a part of the solution. In our transient simulation, it is not possible to specify Re and We *a priori*, since the velocity of the drop is computed as part of the solution. However, once the drag coefficient is known, the Eötvös number and Ohnesorge number can be found by:

$$Eo = \frac{3}{4} We C_d \; ; \; Oh_o = \sqrt{\frac{We}{Re^2}} \tag{19}$$

For a drop translating at a Reynolds number equal to 100 and Weber number equal to 4, with $\rho_d/\rho_o = 0.91$ and $\mu_d/\mu_o = 1$, Dandy and Leal[35] found $C_d = 0.919$ in an unbounded domain. This gives $Eo = 2.75$ and $Oh_o = 0.02$. Our computation was done using a 256×768 grid in a domain 5 and 15 times the initial diameter of the drop in the radial and axial directions, respectively.

The computed Reynolds and Weber numbers differ from those given by Dandy and Leal[35] by less than 1% when the drop reaches steady state. For $\mu_d/\mu_o = 4$ and the same Re, We, ρ_d/ρ_o as in the previous case, Dandy and Leal[35] found $C_d = 1.10$. Our computation was done using $Eo = 3.3, Oh_o = 0.02$, and the same ρ_d/ρ_o and μ_d/μ_o, with the same resolution and domain size as in the previous case. The result gives $C_d = 1.13$, which is approximately 3% higher. This is due to the finite size of our computational domain. Computations using domains of half and twice the original size in the radial direction yield $C_d = 1.19$ and 1.12, respectively.

B. The Boussinesq approximation

Before presenting further computational results, we pause to examine the validity of the Boussinesq approximation. The Boussinesq approximation states that if the density difference is small, density variations are only important when multiplied by gravity. $\Delta\rho$ is therefore no longer an independent parameter and it is sufficient to simulate the breakup for only one value of the density ratio in this limit. Results for other values of $\Delta\rho$ can be obtained by simply rescaling time. For a discussion of the Boussinesq approximation to stratified flows, see, for example, Dahm, Scheil, and Tryggvason[48]. The relative magnitude of the density difference is better expressed by the Atwood number, defined by:

$$A = \frac{\rho_d - \rho_o}{\rho_d + \rho_o} \tag{20}$$

When A is sufficiently small ($\rho_d/\rho_o \to 1$), time and velocities can be scaled by the average static pressure to yield:

$$\hat{t} = \frac{t}{\sqrt{D/(Aa_z)}} \tag{21}$$

$$\hat{u} = \frac{u}{\sqrt{Aa_z D}}; \qquad \hat{v} = \frac{v}{\sqrt{Aa_z D}} \tag{22}$$

The Eötövs number and the Ohnesorge number must also be redefined as:

$$\widehat{Eo} = \frac{\rho_{av} A a_z D^2}{\sigma} \tag{23}$$

$$\widehat{Oh}_o = \frac{\mu_o}{\sqrt{\rho_{av} D \sigma}} \tag{24}$$

where $\rho_{av} = 0.5(\rho_d + \rho_o)$. Note that the constant acceleration appears only as Aa_z instead of a_z alone.

In order to check the validity of the Boussinesq approximation, tests were done for different values of A. In Figure 4, results for $\widehat{Eo} = 72$, $\widehat{Oh}_o = 0.241$, and $\mu_d/\mu_o = 1$ are presented. The computation was done using a 256×768 grid and the size of the computational domain was 5 and 15 times the initial drop diameter in the radial and the axial direction, respectively. The aspect ratio α and the non-dimensionalized centroid velocity $\hat{V}_c$ are plotted versus $\hat{t}$ in (a) and (b), respectively. In each graph, simulations using four values of A are shown: 0.07, 0.11, 0.2, and 0.33, corresponding to the density ratios: 1.15, 1.25, 1.5, and 2.0. The plots confirm that the scaling works well when A is less than about 0.2 to 0.3. The ability to cover this density range by a single simulation is obviously a considerable simplification.

C. Effect of Eo at small Oh

When Oh is small and surface tension is much more important than viscous stresses, Oh has little influence on the breakup and Eo is the only controlling parameter. Here, we present results for different Eo when Oh is small. When a drop is set into motion by a constant body force, the hydrodynamic pressure is higher at the poles and lower at the equator and the drop deforms into an oblate ellipsoid. This deformation is opposed by the surface tension. Depending on the relative strength of the pressure forces and the surface tension, measured by Eo, different breakup modes are observed.

In Figure 5, the effect of Eo is presented for $\rho_d/\rho_o = 10$ and $Oh_o = Oh_d = 0.05$. The simulations are done using a moving coordinate system where the origin is fixed at the centroid of the drop. The domain has dimensions of five and fifteen times the initial drop diameter in the radial and axial directions, respectively. The centroid of the drop is fixed at a position five times the initial drop diameter above the bottom boundary. The evolution of the drop is shown for nine different values of Eo (a to i). In each column, the drop interface is plotted at fixed time intervals.

The separation between two successive drops is equal to the distance that the drop travels during the time interval.

In (a), the drop is shown for $Eo = 12$. As the drop starts falling, the back side becomes flat while the front side retains a rounded shape. After the initial deformation, the drop reaches a steady state and no further change in the drop shape is seen. When Eo is increased to 24 in (b), the drop deformation is more pronounced. Initially, the drop assumes a shape similar to that shown in (a), but then the back of the drop becomes increasingly more convex and eventually the drop deforms into a thin disk-like shape that moves at a nearly steady state. The drop shown in (c) for $Eo = 28.8$ evolves in the same way until it has deformed into a disk-like shape. Then the thickness of the drop near the symmetry axis continues to decrease, and most of the drop fluid moves outward toward the edge of the drop. Finally, the center of the front surface is pushed upward, forming a backward-facing bag. At this stage, most of the drop fluid is contained in the annular-shaped rim. As time progresses, the bag expands both radially outward and vertically upward. Experimental evidence indicates that the drop will eventually break into small drops. The evolution shown in (d) for $Eo = 36$ is very similar to that in (c), displaying a backward-facing bag. The only difference is that the rate of deformation is higher and the backward-facing bag expands more rapidly.

When Eo is further increased to 48 in (e), a different mode of breakup is observed. The initial deformation is not very different from the previous cases, and an indentation develops on the back surface, but instead of deforming into a disk-like shape, the drop remains relatively thick near the symmetry axis and the edge of the drop is swept back in the downstream direction. A large wave then develops on the drop interface and as this wave propagates, the drop deforms in an erratic manner. The evolution of the drop shown in (f) for $Eo = 60$ reveals another mode of deformation. The initial evolution is similar to the previous cases, but the results are different at later times. As the indentation at the top progressively deepens, the drop does not deform into a thin disk-like shape. Instead, the edge of the drop is deflected in the downstream direction and drawn out into a thin film with a blob of drop fluid at the end. The appearance of this film is similar to the skirted drop shapes observed in experimental studies of liquid drops moving at steady state (Wairegi and Grace[49]). The center portion of the drop, however, maintains a convex shape and its thickness at

the symmetry axis stops decreasing. Similar drop deformations are observed at even higher Eo= 72, 96, and 144 as shown in (g), (h), and (i), respectively.

Based on these results, the evolution of drops with $\rho_d/\rho_o = 10$ at a small Oh can be classified into four categories in order of increasing Eo: steady deformation, formation of a backward-facing bag, transient breakup with a complex shape, and stripping or shearing of a film from the edge of the drop. It is evident from Figure 5 that drops breaking up in the backward-facing mode travel a much longer distance than those breaking up in the shear breakup mode. Also note that for the same breakup mode, the rate of drop deformation increases as Eo increases.

In Figure 6, the evolution of a drop with a small density ratio, $\rho_d/\rho_o = 1.15$, is shown for different Eo. Again, values of Ohnesorge numbers, $Oh_o = 0.05$ and $Oh_d = 0.0466$ are chosen so that viscous stresses are small compared to surface tension. The computations were done using a fixed coordinate system. When Eo is small, the drop deforms into an oblate ellipsoid and moves with a steady state shape as shown in (a) for $Eo = 12$. When Eo is increased to 24 (b), the drop deforms more and eventually forms a backward-facing bag as observed for $\rho_d/\rho_o = 10$ in Figure 5(c). In (c), where Eo is 48, the drop moves with an essentially steady convex shape, showing no sign of bag formation. Compared to its high density ratio counterpart shown in Figure 5(e), the overall deformation is reduced. When Eo is 96 in (d), the indentation at the back of the drop deepens continuously until it reaches the front of the drop, creating a forward-facing bag. Eventually, however, the heavier edge falls faster than the thin bag. This formation of a forward-facing bag is different from the shear breakup mode observed in Figure 5(f)-(i), where a significant portion of the fluid remains near the symmetry axis while a thin film is pulled away from the edge. In (e), Eo is further increased to 144. The overall evolution is similar to (d), but the rate of deformation is slightly faster.

In Figure 7, vorticity contours (left) and streamlines with respect to a frame moving with the drop (right) are plotted at a few selected times for the drop shown in Figure 5(c). Most of the vorticity is created at the outer edge of the drop, as expected, and the streamlines show the formation of a large wake behind the drop. The pressure difference between the front stagnation point and the wake causes the formation of the backward-facing bag.

Figure 8 shows vorticity contours (left) and streamlines (right) at a few selected times for the drop shown in Figure 5(f). Although vorticity generated at the drop surface accumulates into a large wake as in Figure 7, the more deformable drop is continuously deformed by the flow (as seen by streamlines crossing its boundary) and the edge is pulled back by the flow. In the last frame, the large wake formed initially separates from the drop, leaving the film to move toward the axis due to the flow around the smaller remaining drop.

In Figure 9, vorticity contours (left) and streamlines (right) are shown for the drop shown in Figure 6(e). Here, the vorticity generated at the interface moves with the drop, forming a dipole that continuously deforms the interface into a forward facing bag.

Figures 10 and 11 show the centroid velocity of the drop V_c plotted versus t^* for the drops shown in Figures 5 and 6, respectively. Since the velocity is non-dimensionalized by $\sqrt{a_z D}$, the graphs for different values of Eo all have the same initial slope. After the initial acceleration, the drop deformation, which depends on Eo, determines the velocity. In Figure 10, drops with low Eo deform less and therefore move faster than drops with high Eo. The lowest Eo drop ($Eo = 12$) asymptotically reaches a steady state velocity, but the other drops all slow down as they start deforming. The $Eo = 24$ drop also reaches a steady velocity. The drops that undergo bag breakup first behave like the $Eo = 24$ drop, but as the bag forms, the drops slow down rapidly. At the very end, the $Eo = 36$ drop speeds up again, as the rim of the drop starts falling independently of the bag. The rest of the drops all slow down rapidly as they are stretched perpendicular to the flow, and all speed up again as the thin film pulled from their edges folds back toward the axis. The results for the small density difference in Figure 11 show a similar trend, but with a few differences. The transient drop ($Eo = 48$) reaches a velocity that is nearly the same as the velocity of the drop moving with a steady deformed shape ($Eo = 12$) and the reduction in speed due to bag breakup is smaller than in Figure 10.

In Figures 12 and 13, the surface area S (normalized by the initial value S_o) is plotted versus t^* for the drops shown in Figures 5 and 6, respectively. The graphs for $\rho_d/\rho_o = 10$ in Figure 12, show that a rapid increase of the surface area takes place when breakup occurs, and that the backward-facing bag breakup mode takes longer than the shear breakup mode. The drops undergoing a shear

breakup show a reduction in surface area when the film moves toward the symmetry axis. The graphs for $\rho_d/\rho_o = 1.15$ in Figure 13 also display a rapid increase of the surface area when the drops break up. However, the drops with the highest Eo show a rapid increase in surface area after the rim starts falling, and the surface area of the drop undergoing bag breakup grows relatively slowly compared to the higher density ratio drops.

D. Effect of Oh

Figure 14 illustrates the effect of the Ohnesorge number (Oh–the non-dimensional viscosity) for drops with a finite density ratio, $\rho_d/\rho_o = 10$. The drops are shown at several stages. Here, Oh_d is equal to Oh_o. The case where Oh_d is different from Oh_o will be discussed in the next section. In the top row (a–c), $Oh = 0.05$, 0.125, and 0.25, from left to right, and $Eo = 28.8$. The $Oh = 0.05$ case (a) has already been shown in Figure 5(c), but is included here for comparison. The initial deformation of all three drops is similar, but whereas the $Oh = 0.05$ drop (a) deforms into a backward facing bag, the other two drops reach a steady state shape. Of those, the less viscous drop (b) is flatter.

In the bottom row (d–f), Eo is increased to 144 and the evolution of the drops is presented for the same three values of Oh as in the top row. In (d), the drop already shown in Figure 5(i) is included for reference. This drop undergoes a so-called shear (or boundary stripping) breakup. The $Oh = 0.125$ drop (e) shows a similar evolution as the drop in (d), although the rate of deformation is reduced slightly. The center portion of the drop still contains a significant amount of drop fluid and formation of a backward-facing bag, which requires the formation of a very thin film of fluid near the symmetry axis, does not occur. In contrast, the center portion of the drop in (f) is drained completely, and the drop forms a backward facing bag.

Based on the results shown in Figure 14, it is clear that increasing both Oh_o and Oh_d simultaneously results in a translation of the boundaries between the breakup modes to higher Eo.

Figure 15 illustrates the effect of viscosity on the initial deformation of drops with $\rho_d/\rho_o = 1.15$. In addition to runs with a finite viscosity, we show simulations with zero viscosity, obtained

by an axisymmetric vortex method (see Dahm, Frieler, and Tryggvason[50]). In the top row, $Eo = 24$ and Oh_o is 0.05, 0.025, 0.01 and 0 from left to right. In all cases, $\mu_d/\mu_o = 1$. While the initial acceleration is dominant, all the drops evolve in the same way. As time progresses, viscosity effects become important and the viscous drops will eventually develop a backward-facing bag due to the formation of a wake. See Figure 6(b) for further deformation of the drop in (a). The inviscid drop (d), on the other hand, loses fluid to a film pulled off its edge. Since this drop does not develop a vortical wake, it does not form a backward facing bag. Similar deformation is also seen for inviscid bubbles[51].

In the bottom row, the limit of zero surface tension, i.e. $Eo = \infty$ is investigated. Since Oh_o is defined with the surface tension in the denominator, it cannot be used as a measure of viscosity in this case. Instead, another non-dimensional number is defined:

$$\hat{\mu} = \frac{\mu_o}{\sqrt{\rho_o \Delta\rho D^3 a_z}} = \frac{1}{\sqrt{Ar}} \tag{25}$$

where Ar is the Archimedes number. Results for three values of $\hat{\mu}$ =0.01021 (e), 0.00513 (f), and 0.00204 (g) are compared with results for $\hat{\mu} = 0$ (h). In all cases, $\mu_d/\mu_o = 1$. From the plots, it can be seen that since there is no surface tension limiting the deformation, all the drops evolve in a similar way: first an indentation forms at the top, then the drops deform into a forward-facing bag with a thick edge. The effect of $\hat{\mu}$ on the overall shape of the drop is relatively small, with the exception of the rollup of the edge which increases as $\hat{\mu}$ is reduced.

E. Effect of the viscosity ratio

The results presented so far are all for drops moving in another fluid that has the same or almost the same viscosity. The effect of the viscosity ratio is shown in Figure 16, where the drops are shown for several values of the governing parameter. In (a) and (b), $\rho_d/\rho_o = 10$ and $Oh_o = 0.05$. Eo is 72 in (a) and 144 in (b). In each row, the drop shape is shown at a fixed t^* for $Oh_d = 0.05$, 0.125, 0.25, and 1.25, increasing from left to right. The evolution of the drops in (a) is qualitatively similar for the three lower values of Oh_d. They all show a shear breakup mode in which a film

of drop liquid is pulled away from the edge of the drop. The drop with the highest Oh_d in the rightmost column, however, has not progressed as far, and will eventually form a forward-facing bag. The comparison in (b), for $Eo = 144$, shows the trend observed in (a). Comparisons for drops with $\rho_d/\rho_o = 1.15$ are presented in (c) and (d). In (c), $Eo = 24$ and $Oh_o = 0.05$. The drops are shown for Oh_d=0.0093, 0.0466, 0.2331, and 1.1656 (from left to right) at $t^* = 63.2$. The drops with the three lower viscosity ratios form a backward-facing bag and the drop deformation is most pronounced when the viscosity ratio is smaller. In contrast, the most viscous drop develops a steady disk-like shape. In (d), $Eo = 144$ and $Oh_o = 0.25$ and the drops are shown for four different values of the drop Ohnesorge numbers, $Oh_d = 0.0093, 0.0466, 0.2331$, and 1.1656 (from left to right) at $t^* = 27.1, 27.1, 46.5$, and 62.0, respectively. The times are not the same because as the viscosity ratio increases, the drops deform much more slowly. Here, the edge of the drop is pulled backward into a thin skirt for the three lower viscosity ratios. The most viscous drop, $Oh_d = 1.1656$, does, on the other hand, form a backward-facing bag.

In Figure 17, the evolution of the centroid velocity is plotted for the drops shown in Figure 16. Initially, while the drops are nearly spherical, acceleration is independent of the viscosity of the drop fluid. As the drops start deforming, they slow down due to increased drag. For the drops with $\rho_d/\rho_o = 10$ shown in (a) and (b), the higher viscosity drops deform more slowly and therefore move faster. At a later time, however, the most viscous drop in (a) forms a backward facing bag and slows down continually. In (c), where the density ratio is lower, the most viscous drop reaches a steady state shape and velocity. The other drops all form bags and are relatively unaffected by changes in the drop viscosity. In (d), the low viscosity drops speed up again, once a skirt has been pulled off their edges, indicating that the skirt has no significant effects on the motion at this stage. The most viscous drop, on the other hand, forms a backward facing bag and continues to slow down.

Increasing the drop viscosity reduces its rate of deformation and in some cases, this can result in different breakup modes, changing a shear breakup to a bag breakup, and a bag breakup to a steady-state shape.

F. Deformation and breakup regime maps

To summarize the results of the various simulations, deformation and breakup maps are presented in Figures 18 and 19. In the maps, we mark the location of each simulation in the Oh_d–Eo plane, using a different symbol, depending on the deformation and breakup mode observed. Similar breakup maps have been used to present experimental results by numerous investigators. Figure 18 shows the result of simulations with $\rho_d/\rho_o = 10$. Three maps are shown (a–c), corresponding to different ambient Ohnesorge numbers.

The map for a relatively small $Oh_o = 0.05$ (a) shows that increasing the magnitude of Eo at a fixed drop Ohnesorge number ($Oh_d = 0.05$) results in the following transitions between the different breakup modes: oblate ellipsoid $\rightarrow$ backward-facing bag mode $\rightarrow$ transient breakup $\rightarrow$ shear breakup mode. Changing Oh_d for a fixed Eo, on the other hand, yields only minor differences in the breakup mode. Increasing Oh_d from 0.05 to 1.25, when Eo is fixed at 28.8, for example, does not change the breakup mode. For $Eo = 72$ and 144, a change from a shear breakup mode to a forward-facing bag mode is observed, as Oh_d is increased from 0.25 to 1.25. The difference between these two breakup modes is, however, not as significant as that between the backward-facing bag and the shear breakup modes.

When Oh_o is increased to 0.125, map (b), the increased viscosity of the surrounding fluid slows the drop down and reduces the rate of deformation. At $Oh_d = 0.05$, increasing Eo yields the following transitions between breakup modes: deformed drop $\rightarrow$ backward-facing bag $\rightarrow$ shear breakup. When the boundaries between these breakup modes are compared to the same Oh_d in map (a), some differences are observed. The backward-facing bag, which was observed at $Eo = 28.8$ in (a), is now seen at $Eo = 36$. At $Eo = 48$, the transient breakup is no longer observed and instead we see a backward-facing bag.

The effect of changing Oh_d at a fixed Eo is also examined in (b). When $Eo = 28.8$, changing Oh_d from 0.05 to 1.25 results in only minor differences. The $Oh_d = 0.05$ drop displays a prolate shape after an initial oscillatory motion but drops with higher Oh_d deform into oblate ellipsoids with an indentation (or a dimple) at the top. At $Eo = 72$, the effect of changing Oh_d is more

significant. Only the $Oh_d = 0.05$ drop shows a shear breakup mode, while the higher Oh_d drops all form a backward-facing bag. At $Eo = 144$, on the other hand, the breakup modes are generally similar to those observed in (a), showing no significant change with Oh_d.

When Oh_o is increased to 0.25 in map (c), the effect of the drop viscosity becomes more significant. At $Eo = 28.8$, four simulations with Oh_d ranging from 0.05 to 1.25 show deformed drops, which are similar to those observed in (b) at the same Eo. At $Eo = 72$, four simulations with Oh_d in the same range all show the formation of a backward-facing bag. This is different from the result in (b) for the same Eo, where the shear breakup mode changes to a backward-facing bag mode as Oh_d increases. At $Eo = 144$, only the $Oh_d = 0.05$ drop shows the shear breakup mode seen in (a) and (b). The $Oh_d = 0.125$ drop deforms into a forward-facing bag and the higher Oh_d drops display a backward-facing bag mode.

In Figure 19, deformation and breakup regime maps are presented for drops with $\rho_d/\rho_o = 1.15$. Three maps are shown in (a)–(c), for ambient fluids with $Oh_o = 0.05, 0.25$, and 1.25. The map for $Oh_o = 0.05$ (a), displays the following transitions between breakup modes as Eo is increased: oblate ellipsoid $\rightarrow$ backward-facing bag $\rightarrow$ oscillating indented drop $\rightarrow$ forward-facing bag. It is clear that increasing Oh_d has no major effects. The only exception is when Oh_d becomes large (> 1) and Eo is relatively low. In this case, the backward-facing bag breakup mode is replaced by a steadily moving indented drop.

When Oh_o is increased to 0.25 (b), a backward-facing bag mode is no longer observed when $Eo = 24$. Instead, a steadily moving indented drop is seen for the Oh_d range investigated. The breakup mode at $Eo = 144$ also changes from a forward-facing bag mode to a skirted drop when Oh_d is small (< 1). A forward-facing bag mode is observed at $Eo = 288$. As in (a), no noticeable effects of changing Oh_d, at a fixed Eo, are observed as long as $Oh_d < 1$. When $Oh_d > 1$, the drop develops a backward-facing bag when $Eo = 144$.

In map (c), $Oh_o = 1.25$ and the high viscosity prevents nearly all deformation. When $Eo = 24$, the drop remains an oblate ellipsoid but for $Eo = 144$, the drops develop an indentation at the back. The indentation of the more viscous drop ($Oh_d = 1.1656$) deepens continuously until it reaches the bottom surface of the drop, forming a vortex ring.

G. Conclusions

The deformation and breakup of axisymmetric drops, accelerated by a constant body force, have been studied by numerical simulations. Results are presented for two density ratios, $\rho_d/\rho_o = 1.15$ and $\rho_d/\rho_o = 10$. For the lower density ratio, the Boussinesq approximation is valid and the results therefore apply for other low density ratios by the simple rescaling discussed in section III. For low Ohnesorge numbers, the Eötvös number and the density ratio are the main controlling parameters. At low density ratios the drop deforms, but does not break up for Eo less than about 18. For $18 < Eo < 36$ (approximately), the drop breaks up by the formation of a backward facing bag. Transient breakup is observed for Eo around 48, and at Eo larger than about 60, the drop evolves into a forward facing bag.

The formation of a forward-facing bag takes place very quickly (the drop has moved only 3–4 times its initial diameter when the bag is formed) and is essentially an inviscid phenomenon. The formation of a backward-facing bag, on the other hand, takes significantly longer (the drop has moved 8–10 times its initial diameter). A comparison with results obtained by an inviscid vortex method shows that the backward facing bag is a viscous phenomenon, due to the formation of a low pressure wake behind the drop. Furthermore, the surface area of the drop increases at a faster rate in the forward-facing bag mode.

As Oh is increased, the effect of the viscosity reduces the rate of deformation. At low Eo, while the drop flattens, its center does not drain completely and backward-facing bag does not form. As Eo becomes larger, the edges of the drop are pulled outward and sheared off, leading to a "skirted" drop.

When Oh becomes very large, the drop deforms into an oblate ellipsoid at low Eo. At high Eo, baroclinically generated vorticity causes indentation of the back of an accelerated drop, but rapid diffusion of vorticity prevents the roll-up observed for lower Oh. As this indentation continues to grow, the drop finally breaks into a torus. Similar evolution has been seen in simulations of initially oblate drops in Stokes flow (Koh and Leal[31], Pozrikidis[33]).

The effect of the viscosity ratio is small when Oh_o is small. Although there are differences in

the detailed shape of the drop, the overall evolution is generally similar when Oh_d is varied at fixed Eo and Oh_o unless Oh_d is very large. For larger Oh_o, the effect of the viscosity ratio becomes more significant and as Oh_d increases, the boundaries between the different breakup modes are moved to higher Eo.

At higher density ratio ($\rho_d/\rho_o = 10$) the evolution is similar to the low density ratio case and the effect of the governing parameters is also similar. There are, however, a few important differences. At large Eo, the forward facing bag seen for the low density case is replaced by a shear breakup mode where the edge of the drop is pulled in the downstream direction, forming a blob of drop fluid connected to the main drop by a thin film. The skirted drop in the low density ratio case is similar in shape (except that no blob was formed). The skirt, however, appears only at a relatively higher Oh and grows slowly once it has formed. In contrast, the shear breakup mode in the higher density ratio case occurs across the Oh range investigated here. The boundaries between the breakup modes at low Oh remain essentially the same as for the low density ratio case.

In most practical combustion systems, the density difference between the liquid fuel and the high pressure gas is considerably smaller than at atmospheric temperature and pressure. For diesel engines, $\rho_d/\rho_o = 32 - 53$, for example, (see Heywood[52]) and ρ_d/ρ_o of order unity is common in rocket motors. Nearly all experimental studies of secondary breakup of drops, however, have been done at atmospheric pressures. The present study approaches the breakup problem from the small density ratio limits, thus complementing previous work. Covering the gap for density ratios between those studied here and the experiments is within the range of present computational capabilities, but requires considerably longer computational times.

IV. IMPULSIVE ACCELERATION

The breakup of drops subject to impulsive acceleration has been examined for two density ratios ($\rho_d/\rho_o = 1.15$ and ($\rho_d/\rho_o = 10$). As shown in the last section, a simple rescaling of time allows the results for the lower density ratios to be applied for density ratios up to about 2. The evolution has been examined for several Reynolds and Weber numbers.

A. Results

Figure 20 shows the evolution of drops with $We = 2.73$, 13.7, 27.4, 54.7, and ∞. The density ratio is $\rho_d/\rho_o = 1.15$, the Reynolds number is fixed at 331, and the viscosity ratio is 1. The computation was done using a 128×256 grid and the drop contours are shown at selected times. The low Weber number drop in (a) oscillates due to the high surface tension. As We is increased to 13.7, the drop starts to develop an indentation at the top as shown in (b) but as it falls, the momentum of the drop decreases and the surface tension causes it to oscillate. The drop shown in (c) for $We = 27.4$ also deforms into an indented ellipsoid initially. The indentation deepens progressively and later meets the bottom of the drop interface, forming a forward-facing bag as observed in the continuous acceleration case. However, since there is no force to maintain the motion, the drop eventually resumes its initial shape. The drop with $We = 54.7$ in (d), on the other hand, shows increased initial deformation which results in a bigger rim that is connected by a forward-facing bag. In case of zero surface tension in (e), the drop displays a roll-up of the interface. A similar roll-up has been observed in the constant acceleration cases for drops with no surface tension.

In Figure 21, the normalized aspect ratio, centroid velocity, and surface area are plotted versus t^* in (a)–(c), respectively for the drops shown in Figure 20. The aspect ratio plot shows shape oscillation for the two lower values of We. For higher We, the aspect ratio decreases monotonically to zero as the indentation deepens progressively. The velocity plot in (b) shows a rapid decline initially. Later, the velocity of the drops with $We = 2.73$ and 13.7 decreases but with fluctuations. The velocities of the drops with three higher Weber numbers decrease monotonically until it reaches a minimum and starts to increase again. The surface area plot in (c) show the effect of We on deformation: As We increases, the slope of the curve increases.

In Figure 22, the evolution of a drop with $\rho_d/\rho_o = 10$ is shown for $Re = 242$ and $\mu_d/\mu_o = 1.25$. Results for ten $We = 3.74, 12.5, 18.7, 28.1, 37.4, 46.8, 56.1, 74.8, 93.5$ and ∞ are compared. The computation was done using a 256×512 grid. The effect of increasing We is generally similar to the small density ratio case. The drop in (a) with $We = 3.74$ shows oscillatory deformation.

The drops with $We = 12.5$ and 18.7 in (b) and (c) develop an indentation at the top and deform into a forward-facing bag shape. As the velocity continues to decrease, the deformation of the drops eventually is reduced. At later stages of the deformation, the drops assume a shape concave to the incoming flow or a backward-facing bag. The Weber numbers for the drops are in the range where a bag breakup mode is observed experimentally for higher density ratios. In order for the backward-facing bag to grow, higher initial momentum is necessary. The drop in (d) with $We = 28.1$ shows more clearly the development of a backward-facing bag. The results for even higher Weber numbers shown in (e)–(i) show, on the other hand, the formation of a forward-facing bag. The drop with zero surface tension in (j) also displays a forward-facing bag. In this case small scale irregularities are observed both on the edge and on the top surface of the drop.

The aspect ratio, centroid velocity and surface area of some of the drops shown in Figure 22 are plotted versus t^* in Figure 23. The aspect ratio plot displays an oscillation of the drop with the lowest We and monotonic decrease for the other drops. When the drops with $We = 12.5$ and 18.7 start to resume their initial shape, an abrupt increase in the aspect ratio is observed. The velocity plot shows a monotonic decline for all We shown. Unlike the result for the small density ratio shown in Figure 21(b), no fluctuations occurs. The surface area plot shows that the rate of deformation increases with We.

In Figure 24 and 25, vorticity contours (left) and streamlines (right) at selected times are plotted along with the drop contour for the $We = 28.1$ and $We = 93.5$ drops shown in Figure 22(d) and (i) respectively. In both cases, the vorticity plots show that most of the vorticity is created at the outer edge of the drop, as expected. The streamline pattern for the $We = 28.1$ drop shows that the backward-facing bag is stretched upward in the downstream direction when the wake in the downstream detaches from the drop. On the other hand, the closed streamlines around the $We = 93.5$ drop suggests that the drop moves as a vortex ring, forming a forward-facing bag.

In order to see the effect of the viscosity of the surrounding fluid, another computation has been done for $Re = 387$. The results are presented in Figure 26 for the same set of Weber numbers ($We = 3.74, 12.5, 18.7, 28.1, 37.4, 46.8, 56.1, 74.8, 93.5$, and ∞) as in Figure 22. ρ_d/ρ_o is 10 and μ_d/μ_o is 2. Despite the change in the Reynolds number and the viscous ratio, the overall evolution

of the drops is very similar. The only difference is in the small structure of the drop contour. The aspect ratio, centroid velocity, and surface area plotted versus t^* for selected cases in Figure 27 also display very similar behavior as in Figure 23.

Two other series of computations are shown for Reynolds numbers, $Re = 121$ in Figure 28 and $Re = 60.5$ in Figure 29. The viscosity ratios, μ_d/μ_o, are 0.625 and 0.3125, respectively. The density ratio is 10 in both cases. Again, results are presented for the same set of Weber numbers as used in Figures 22 and 26. Comparing the results in Figures 22, 26, 28, and 29, it is clear that progressively higher Weber numbers are necessary in order to observe the same mode of deformation, as the Reynolds number decreases. The translation of the boundaries between different deformation modes—oscillation, backward-facing bag, and forward-facing bag—to higher We is clearly due to the increased viscous dissipation.

In Figure 30, the effect of drop viscosity is shown for drops with $\rho_d/\rho_o = 10$ and $Re = 242$. The figures in each frame denotes the dimensionless time when the drop is plotted. In the top row, four cases are compared for different drop viscosity (represented by the Reynolds number based on drop properties) at a fixed Weber number, $We = 28.1$. As the drop viscosity is increased from left to right by an order of 10^3, the drop deformation is greatly reduced. The least viscous drop with $Re_d = 1.935 \times 10^3$ clearly shows the formation of a backward-facing bag, while the most viscous drop with $Re_d = 1.935$ remains in an oblate shape. In the middle row, a similar comparison is made for $We = 56.1$. Again, by increasing the drop viscosity, the drop deformation is reduced and the drop changes from a forward-facing bag to an oblate drop. The result for $We = 93.5$ drops shown in the bottom row also displays a similar trend.

Figure 31 presents another study of the effect of viscosity ratio at $Re = 387$ and $\rho_d/\rho_o = 10$. The overall trend is similar to that observed in Figure 30 for $Re = 242$. As the drop viscosity is increased at a fixed Weber number, the large deformation in either backward-facing bag or forward-facing bag mode disappears.

In Figure 32, a breakup map is shown to summarize the deformation of drops with $\rho_d/\rho_o = 10$ and $Re_d = 1935$. The horizontal and vertical axes represent the Reynolds number and the Weber number based on the ambient fluid, respectively. The various breakup modes are denoted by

different symbols. When the Weber number is low, surface tension prevents large deformation so the drop only oscillates. As the Weber number increases past a critical value (approximately 16), a backward-facing bag starts to emerge at higher Reynolds numbers first. When the Weber number is higher than approximately 30, the drops break up in a backward-facing bag mode for low Reynolds numbers and in a forward-facing bag mode at high Reynolds numbers. The transitions from the backward-facing bag mode to the forward-facing bag mode occur at progressively lower Reynolds numbers as the Weber number increases. This trend continues until the Weber number reaches approximately 100 and all drops break up in the forward-facing bag mode for the Reynolds number range examined. Finally, when the surface tension vanishes ($We \to \infty$), the strong shear due to the outside flow peels off the drop interface and shear breakup is observed when the Reynolds number is greater than 100.

B. Conclusion

To study the characteristics of impulsively accelerated drops, numerical simulations have been done for two density ratios, 1.15 and 10. These values of ρ_d/ρ_o are lower than those used in most of the experimental investigations of the drop breakup due to impulsive disturbance and therefore of more relevance to high pressure sprays. At low We (< 10), the drops display oscillatory deformation. As We increases, an indentation develops at the top of the drops. Since the velocity and the aerodynamic forces causing deformation continue to decrease, the surface tension eventually takes over and the drops resume the initial spherical shape.

The formation of a backward-facing bag is observed only for a finite density ratio (10). The absence of a growing backward-facing bag confirms the general observation that the disruptive aerodynamic force must be imposed for a sufficiently long duration of time, as in the case of a continuously accelerating drop (for example, see Sadhal, Ayyaswamy, and Chung[28]). In our simulations, the velocity decreases too fast for the backward facing bag to grow when the density ratio is low.

When We is further increased, the initial deformation is so large that a forward-facing bag is

formed. It is expected that in order to obtain a shear breakup where a film is stripped from the main drop, simulations for even higher density ratio is necessary.

V. SHEAR BREAKUP OF IMMISCIBLE FLUID INTERFACES

To start looking at the shear breakup of jets, several two-dimensional simulations of immiscible periodic shear layers were done. The Reynolds numbers were selected to be sufficiently high so that the initial instability was well predicted by inviscid theory, but viscous effects became important at larger amplitude. The linear stability analysis predicts that surface tension stabilizes short waves and yields a wavelength with a largest linear growth rate (most unstable wave). Generally, it was found that the inviscidly most unstable mode saturates quickly and perturbations of longer wavelength are the ones that grow to larger amplitude. Exactly which wavelength is the most dangerous one depends on the Reynolds number. Two sets of simulations were conducted, one at zero density differences and the other at density ratios of ten. For zero stratification, surface tension prevents Kelvin-Helmholtz roll-up as seen for miscible fluids and fingers of one fluid penetrate the other fluid. The slope of these fingers depends on the nondimensional wavelength (Weber number). While viscous effects limit the growth of the fingers at low Weber numbers, high Weber number fingers can become very long. At even higher Weber numbers the interface start to exhibit a behavior more similar to the classical nonlinear Kelvin-Helmholtz instability and rollup. The transition, however, is complex and intermediate states where the interface folds over once before being stretched into a long finger were found, for example. At larger density ratios, the evolution is no longer symmetric and waves of the heavy liquid grow into the lighter one. As for zero stratification, waves with wavelength close to the most unstable one are generally stabilized at large amplitude by viscous effects but longer wavelengths lead to a "wave breaking" where a finger of the heavy fluid is pulled into the lighter fluid. Even in the two-dimensional simulations, these fingers eventually break down into drops. The slope of the "fingers" and the size of the resulting drops depend on the nondimensional wavelength (Weber number).

These preliminary studies have been described in G. Tryggvason and S.O. Unverdi. "The

Shear Breakup of an Immiscible Fluid Interface" published in "Fluid Dynamics at Interfaces" (Ed. W. Shyy) Cambridge University Press, 1999. A more detailed examination of the breakup of immiscible fluid interfaces has been conducted under an AASERT contract (F49620-97-1-0525).

VI. THREE-DIMENSIONAL SIMULATIONS OF DROP BREAKUP

While axisymmetric simulations capture well the initial evolution of drops that are breaking up, the eventual breakup is a fully three-dimensional process. During bag breakup, the rim generally undergoes Rayleigh-Taylor instability and forms drops that are considerably larger than drops that are formed when the bag breaks. The sheet that is pulled from the edge of drops undergoing shear breakup is also likely to become three-dimensional before it breaks into drops. In some cases, particularly at low Eötvös and Weber numbers and in the transition zone between a bag and a shear breakup the process can be fully three-dimensional right from the start. To begin examining the three-dimensional aspects of drop breakup, several computations have been done of drops accelerated by a constant body force in both the bag and the shear breakup mode. Drops in bag breakup mode become three-dimensional quickly, but so far, the computations have not shown the development of three-dimensional structures in the shear breakup mode.

Figure 33 shows four frames from one simulation of a drop undergoing bag breakup and the development of three-dimensional instabilities. The computation is done in a fully periodic domain on a 64^3 grid. To resolve the drop as well as possible, it is taken to be 0.4 times the size of the domain. The density ratio here is 2, and the Ohnesorge numbers are $Oh_d = 0.5$ and $Oh_o = 0.3536$. The Eötvös number is $Eo = 160$ and since the fluids are very viscous the drop breaks up in a bag-breakup mode. In the first frame the drop has developed an indentation at the back that grows until the drop consists of a "bowl" with a thin bottom and a thick rim. The bottom of the "bowl" is pushed back by the difference between the stagnation pressure at the front of the drop and the low pressure in the wake. As the bag expands, the rim becomes unstable and starts breaking up into few relatively large drops. The formation of small scales eventually results in structures that are not well resolved, and the computations are terminated when this happens. To compute the

breakup for lower Ohnesorge numbers, finer resolution is necessary.

VII. SIMULATIONS OF HEAT TRANSFER DURING BREAKUP

The ultimate reason for atomizing a fuel jet is to increase the evaporation rate of the fuel. Before evaporation, the fuel must heat up. As fuel drops break up, their surface area increases greatly and therefore the heat transfer to the drop. To examine the heat transfer, several simulations have been done that include the solution of the unsteady energy equation. If heat generation due to viscous friction and radiation heat transfer is neglected, the energy equation is:

$$\frac{\partial \rho c_p T}{\partial t} + \nabla \cdot (\rho c_p T) = \nabla \cdot k \nabla T. \tag{26}$$

This equation is solved on a fixed grid by an explicit second order method in the same way as the momentum equation. Figure 34(a) shows average temperature of the three drops versus time and Figure 34(b) shows the normalized heat transfer rate, obtained by differentiating the data in Figure 34(a) and dividing by temperature:

$$\tilde{h} = \frac{1}{T_\infty - T} \frac{dT}{dt} \tag{27}$$

The Ohnesorge number is 0.05, $\rho_d/\rho_o = 1.15$, $\mu_d/\mu_o = 0.2$, $c_{p_d}/c_{p_o} = 1$, $k_d/k_o = 0.2$, and the Eötvös number is 2.4, 24, and 144. For the lowest Eo, the drop remains almost spherical, for $Eo = 24$ the drop forms a backward facing bag, and for the highest Eo, the drop evolves in the shear breakup mode. Since the highest Eo drop has reached the temperature of the ambient fluid by time 20, the heat transfer coefficient has not been computed after that time. Initially the drops gain heat at approximately the same rate, but as they start to deform, the rate depends strongly on the breakup mode. The heat transfer rate is slowest for the nearly spherical drop and quickly increases as the Eo increases. For the spherical drop the heat transfer rate decreases as the thermal boundary layer grows and then oscillates weakly as the drop shape oscillates. The heat transfer coefficient for the drop that evolves into a bag-breakup mode first decreases and then increases slightly. The heat transfer for the higher Eo drops initially increases rapidly as the drop deforms,

and even though it drops again, it still remains about three times higher than for the lower Eo drops.

The temperature field and the drop contour are plotted for all three cases in Figure 35. The spherical drop is plotted at $t = 28$, the bag-breakup drop at $t = 28$, and the shear breakup drop at $t = 4$. The temperature field around the spherical drops shows that recirculation inside the drops leads to a ring of cold fluid near the front of the drop and a steep temperature gradient near the front of the drop. As the drop heats up, the ambient fluid cools down and a cold thermal wake extends downstream from the drop. The temperature field inside the drop undergoing bag breakup is very different. There is essentially no recirculation inside the drop and the coldest fluid is at the centerline of the drop. Since there is a large wake behind the drop, the cold thermal wake is much larger than for the low Eo drop. The drop undergoing shear breakup has only a small thermal wake, but the large deformation of the drop leads to a large heat transfer rate. As the results in section C showed the rate of increase of surface area increases greatly as Eo is increased. However, the flow field is also different and convective heat transfer changes. How much of the increased heat transfer can be attributed to increased surface area and how much to increased convection has not been examined in detail yet.

FIGURES

FIG. 1. Schematic illustration of the computational setup.

FIG. 2. Resolution test. The breakup of a drop computed using a 256×512 grid (left) and a 512×1024 grid (right). $\rho_d/\rho_o = 1.15$, $Eo = 144, Oh_o = 0.05, Oh_d = 0.0466$. The drop shape is plotted every $\Delta t_p^* = 3.873$.

FIG. 3. Resolution test. Aspect ratio and centroid velocity plotted versus t^*. Results using three different grids, 128×256, 256×512, and 512×1024, are shown. $\rho_d/\rho_o = 1.15$, $Eo = 144, Oh_o = 0.05, Oh_d = 0.0466$.

FIG. 4. Test of the Boussinesq approximation. Aspect ratio and centroid velocity plotted versus $\hat{t}$. Results are shown for four different Atwood numbers: 0.07, 0.11, 0.2, and 0.33. The corresponding density ratios are 1.15, 1.25, 1.5, and 2.0. $\widehat{Eo} = 72$, $\widehat{Oh_o} = 0.241$, and $\mu_d/\mu_o = 1$.

FIG. 5. Effect of Eo on the deformation of drops with $\rho_d/\rho_o = 10$. $Oh_o = Oh_d = 0.05$. The simulations are done using a 256×768 grid for a moving computational domain of dimensions 5×15 the initial drop diameter. The boundaries of the column do not indicate the actual boundaries of the computational domain. The gap between two successive drops in each column represents the distance the drop travels at a fixed time interval and the last interface is plotted at t^* = (a) 11.19; (b) 15.82; (c) 14.85; (d) 13.83; (e) 11.19; (f) 7.15; (g) 7.83; (h) 6.78; (i) 5.54.

FIG. 6. Effect of Eo on the deformation of drop with $\rho_d/\rho_o = 1.15$. $Oh_o = 0.05, Oh_d = 0.0466$. The simulations are done using a 256×1280 grid in (b) and (c) and a 256×768 grid in (a), (d), and (e). The fixed computational domain has a dimension of 5×15 the initial drop diameter in (b) and (c) and 5×25 the initial drop diameter in (a), (d), and (e). The dashed line in (a), (d), and (e) represents the actual bottom boundary of the computational domain. The gap between two successive drops in each column represents the distance the drop travels at a fixed time interval and the last interface is plotted at t^* = (a) 44.72; (b) 79.06; (c) 89.44; (d) 37.94; (e) 38.73.

FIG. 7. Vorticity contours (left) and streamlines (right) for the drop in Figure 5(c). $\rho_d/\rho_o = 10$, $Eo = 28.8$, $Oh_o = Oh_d = 0.05$. The results are shown for four selected times.

FIG. 8. Vorticity contours (left) and streamlines (right) for the drop in Figure 5(f). $\rho_d/\rho_o = 10$, $Eo = 60$, $Oh_o = Oh_d = 0.05$. The results are shown for five selected times.

FIG. 9. Vorticity contours (left) and streamlines (right) for the drop in Figure 6(e). $\rho_d/\rho_o = 1.15$, $Eo = 144$, $Oh_o = 0.05$, $Oh_d = 0.0466$. The results are shown for four selected times.

FIG. 10. Centroid velocity versus t^* for the drops shown in Figure 5. The results are presented for $Eo = 12, 24, 28.8, 36, 48, 60, 72, 96$, and 144. $\rho_d/\rho_o = 10$, $Oh_o = Oh_d = 0.05$.

FIG. 11. Centroid velocity versus t^* for the drops shown in Figure 6. The results are presented for $Eo = 12, 24, 48, 96$, and 144. $\rho_d/\rho_o = 1.15$, $Oh_o = 0.05$, $Oh_d = 0.0466$.

FIG. 12. Normalized surface area versus t^* for the drops shown in Figure 5. The results are presented for $Eo = 12, 24, 28.8, 36, 48, 60, 72, 96$, and 144. $\rho_d/\rho_o = 10$, $Oh_o = Oh_d = 0.05$.

FIG. 13. Normalized surface area versus t^* for the drops shown in Figure 6. The results are presented for $Eo = 12, 24, 48, 96$, and 144. $\rho_d/\rho_o = 1.15$, $Oh_o = 0.05$, $Oh_d = 0.0466$.

FIG. 14. Effect of Oh for drops with $\rho_d/\rho_o = 10$. The drop evolution is shown for three $Oh_o = Oh_d = 0.05$, 0.125, and 0.25. In the upper row (a)–(c), Eo is fixed at 28.8 and the time interval between successive interfaces, Δt_p^*, is 2.121. In the lower row (d)–(f), Eo is 144 and Δt_p^* is 0.791.

FIG. 15. Effect of Oh on the initial deformation of drops with $\rho_d/\rho_o = 1.15$. In all cases, $\mu_d/\mu_o = 1$ and the time intervals between successive interfaces, $\Delta t_p^* = 1.581$. In the upper row (a)–(d), $Eo = 24$ and in the lower row (e)–(h), $Eo = \infty$ (zero surface tension). The viscous simulations (a)–(c) and (e)–(g) were done using a 128×384 grid. (d) and (h) were done using an inviscid vortex method.

FIG. 16. Effect of the viscosity ratio. In each row, the drops at a late time are shown for different values of the drop viscosity while other parameters are fixed. In (a) and (b), $Oh_d = 0.05, 0.125, 0.25$, and 1.25 (from left to right). In (c) and (d), $Oh_d = 0.0093, 0.0466, 0.2331$, and 1.1656 (from left to right).

FIG. 17. Centroid velocity versus t^* for the drops shown in Figure 16.

FIG. 18. Deformation and breakup regime maps for $\rho_d/\rho_o = 10$. Three maps are shown for $Oh_o = 0.05$, 0.125 and 0.25. In each map, the horizontal and vertical axes are Oh_d and Eo, respectively.

FIG. 19. Deformation and breakup regime maps for $\rho_d/\rho_o = 1.15$. Three maps are shown for $Oh_o = 0.05, 0.25$ and 1.25. In each map, the horizontal and vertical axes are Oh_d and Eo, respectively.

FIG. 20. Evolution of impulsively started drops with $Re = 331$, $\rho_d/\rho_o = 1.15$, and $\mu_d/\mu_o = 1$. Results for five We are shown as denoted by the numbers below the figures. The numbers inside the frames denote t^* when the interfaces are plotted. The computations were done on a 128×256 grid.

FIG. 21. Non-dimensionalized aspect ratio, centroid velocity, and surface area plotted versus t^* for the drops shown in Figure 20. Results for five $We = 2.73$, 13.7, 27.4, 54.7, and ∞ are compared. $Re = 331$, $\rho_d/\rho_o = 1.15$ and $\mu_d/\mu_o = 1$.

FIG. 22. Evolution of impulsively started drops with $Re = 242$, $\rho_d/\rho_o = 10$, and $\mu_d/\mu_o = 1.25$. Results for ten We are shown as denoted by the numbers below the figures. The numbers next to the drops denote t^* when the interfaces are plotted. The centroid of the drops in a column are separated by a fixed distance. The gap between two successive drops in a column does not represents the distance the drop travels during the time interval. The computations were done on a 256×512 grid.

FIG. 23. Non-dimensionalized aspect ratio, centroid velocity, and surface area plotted versus t^* for selected cases of the drops shown in Figure 22. Results for five $We = 3.74$, 12.5, 18.7, 37.2, and 93.5 are compared. $Re = 242$, $\rho_d/\rho_o = 10$ and $\mu_d/\mu_o = 1.25$.

FIG. 24. Vorticity contours (left) and streamlines (right) for the drop shown in Figure 22(d).

FIG. 25. Vorticity contours (left) and streamlines (right) for the drop shown in Figure 22(i).

FIG. 26. Evolution of impulsively started drops with $Re = 387$, $\rho_d/\rho_o = 10$, and $\mu_d/\mu_o = 2$. Results for ten We are shown as denoted by the numbers below the figures. The numbers next to the drops denote t^* when the interfaces are plotted. The centroid of the drops in a column are separated by a fixed distance. The gap between two successive drops in a column does not represents the distance the drop travels during the time interval. The computations were done on a 256×512 grid.

FIG. 27. Non-dimensionalized aspect ratio, centroid velocity, and surface area plotted versus t^* for selected cases of the drops shown in Figure 26. Results for five $We = 3.74$, 12.5, 18.7, 37.2, and 93.5 are compared. $Re = 387$, $\rho_d/\rho_o = 10$ and $\mu_d/\mu_o = 2$.

FIG. 28. Evolution of impulsively started drops with $Re = 121$, $\rho_d/\rho_o = 10$, and $\mu_d/\mu_o = 0.625$. Results for ten We are shown as denoted by the numbers below the figures. The numbers next to the drops denote t^* when the interfaces are plotted. The centroid of the drops in a column are separated by a fixed distance. The gap between two successive drops in a column does not represents the distance the drop travels during the time interval. The computations were done on a 256×512 grid.

FIG. 29. Evolution of impulsively started drops with $Re = 60.5$, $\rho_d/\rho_o = 10$, and $\mu_d/\mu_o = 0.3125$. Results for ten We are shown as denoted by the numbers below the figures. The numbers next to the drops denote t^* when the interfaces are plotted. The centroid of the drops in a column are separated by a fixed distance. The gap between two successive drops in a column does not represents the distance the drop travels during the time interval. The computations were done on a 256×512 grid.

FIG. 30. Drop viscosity effect on the deformation of drops with $\rho_d/\rho_o = 10$ and $Re = 242$. The number in each frame denotes the dimensionless time when the drop is plotted.

FIG. 31. Drop viscosity effect on the deformation of drops with $\rho_d/\rho_o = 10$ and $Re = 387$. The number in each frame denotes the dimensionless time when the drop is plotted.

FIG. 32. Breakup mode map for impulsively started drops with $\rho_d/\rho_o = 10$ and $Re_d = 1935$.

FIG. 33. Three-dimensional simulation of drop breakup. $\rho_d/\rho_o = 2$, $Eo = 160$, $Oh_d = 0.5$, and $Oh_o = 0.3536$.

FIG. 34. Simulations of heat transfer during drop breakup for $Eo = 2.4, 24$, and 144. Average temperature of the drops (a) and normalized heat transfer rate (b) are plotted versus time. $Oh = 0.05$, $\rho_d/\rho_o = 1.15$, $\mu_d/\mu_o = 0.2$, $c_{p_d}/c_{p_o} = 1$, and $k_d/k_o = 0.2$

FIG. 35. Temperature field and drop contour are plotted for the drops shown in Figure 34 at selected times.

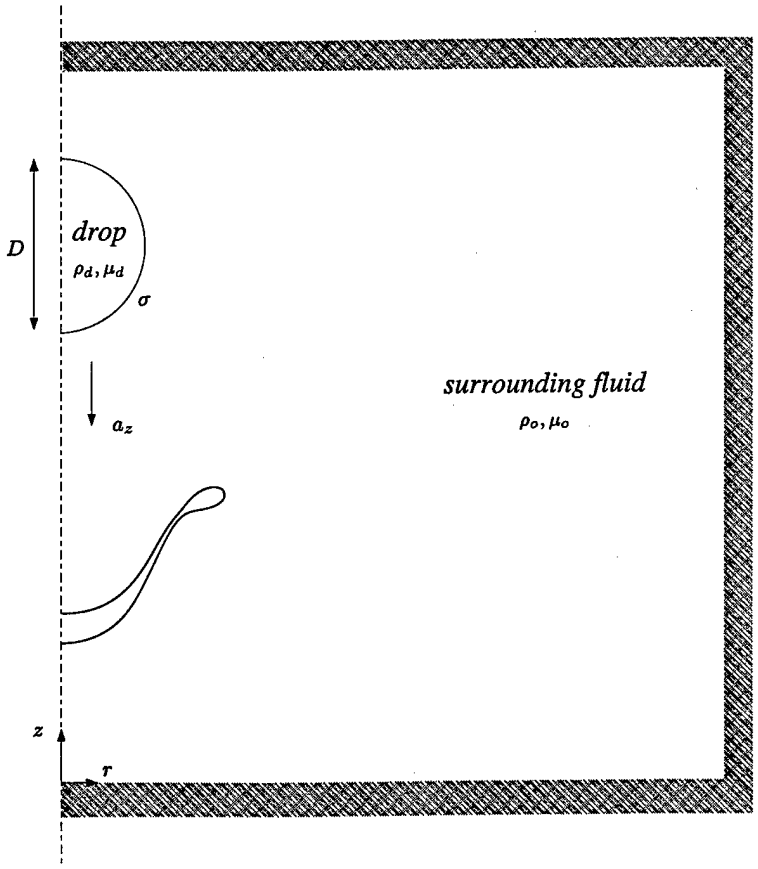
D
drop
ρ_d, μ_d
σ
a_z
surrounding fluid
ρ_o, μ_o
z
r

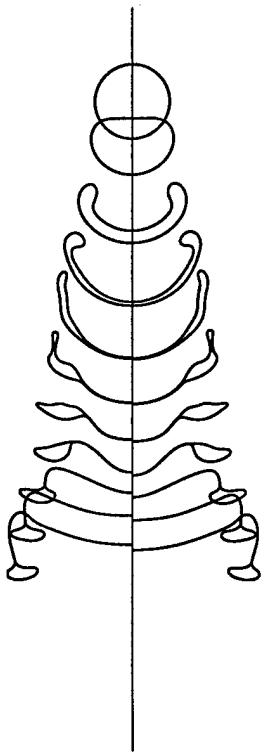

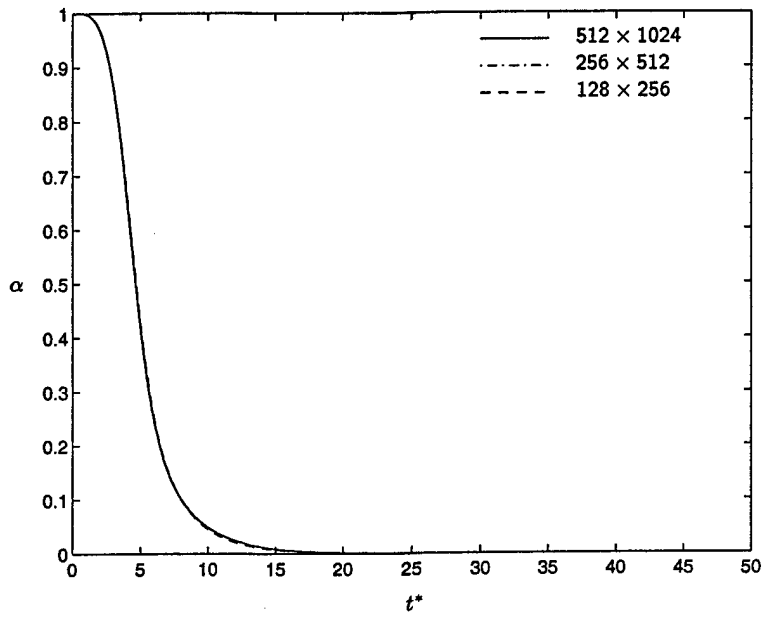

(a) aspect ratio

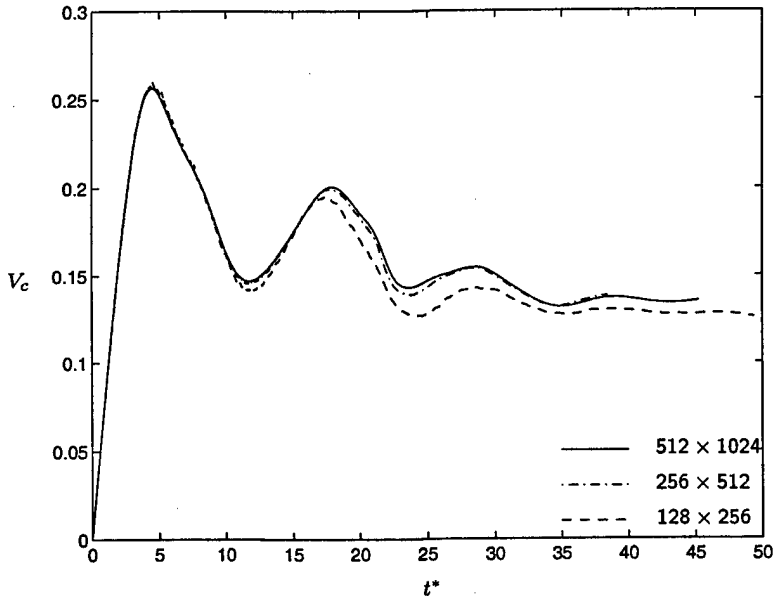

(b) centroid velocity

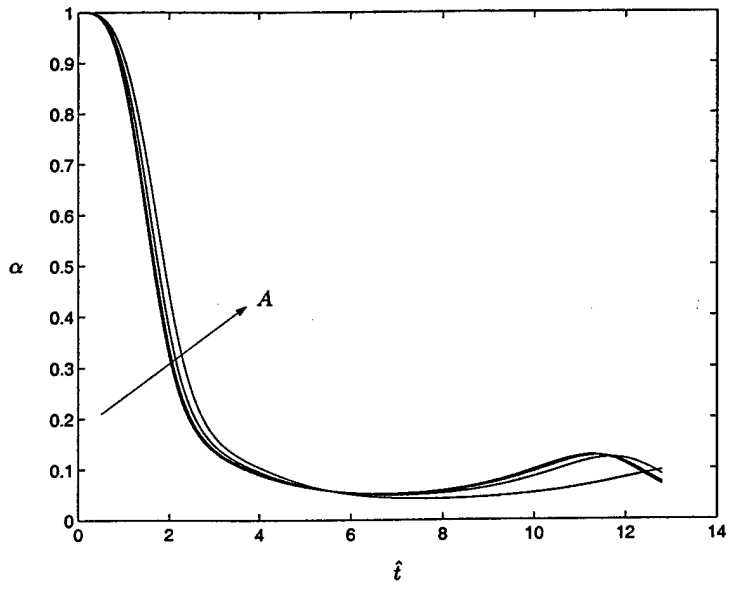

(a) aspect ratio

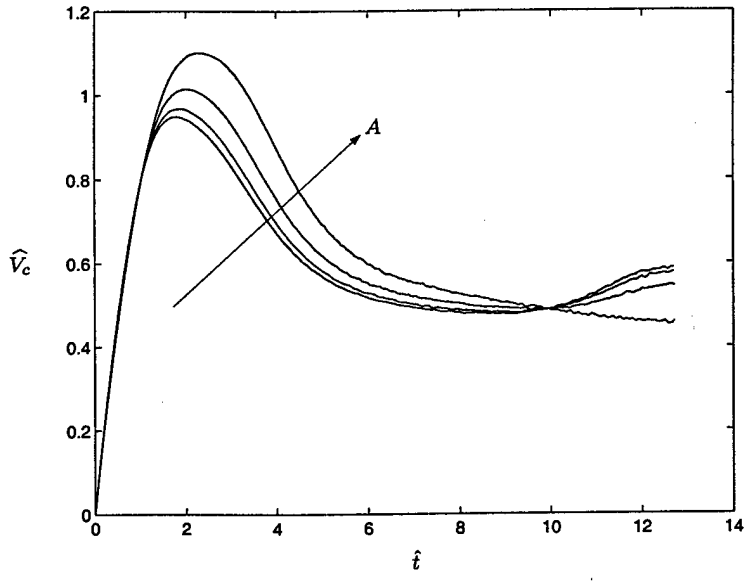

(b) centroid velocity

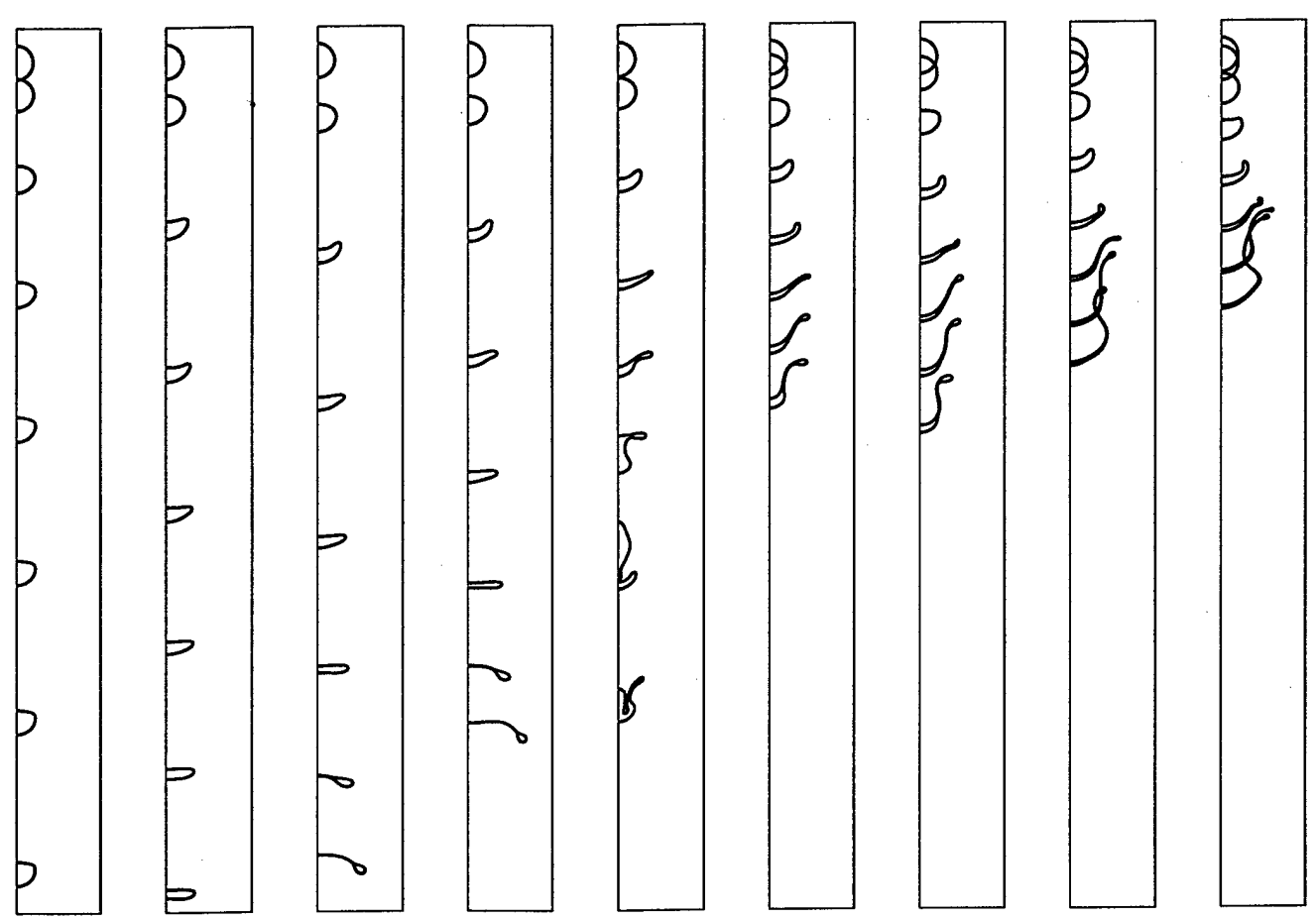

(a) $Eo = 12$ (b) $Eo = 24$ (c) $Eo = 28.8$ (d) $Eo = 36$ (e) $Eo = 48$ (f) $Eo = 60$ (g) $Eo = 72$ (h) $Eo = 96$ (i) $Eo = 144$

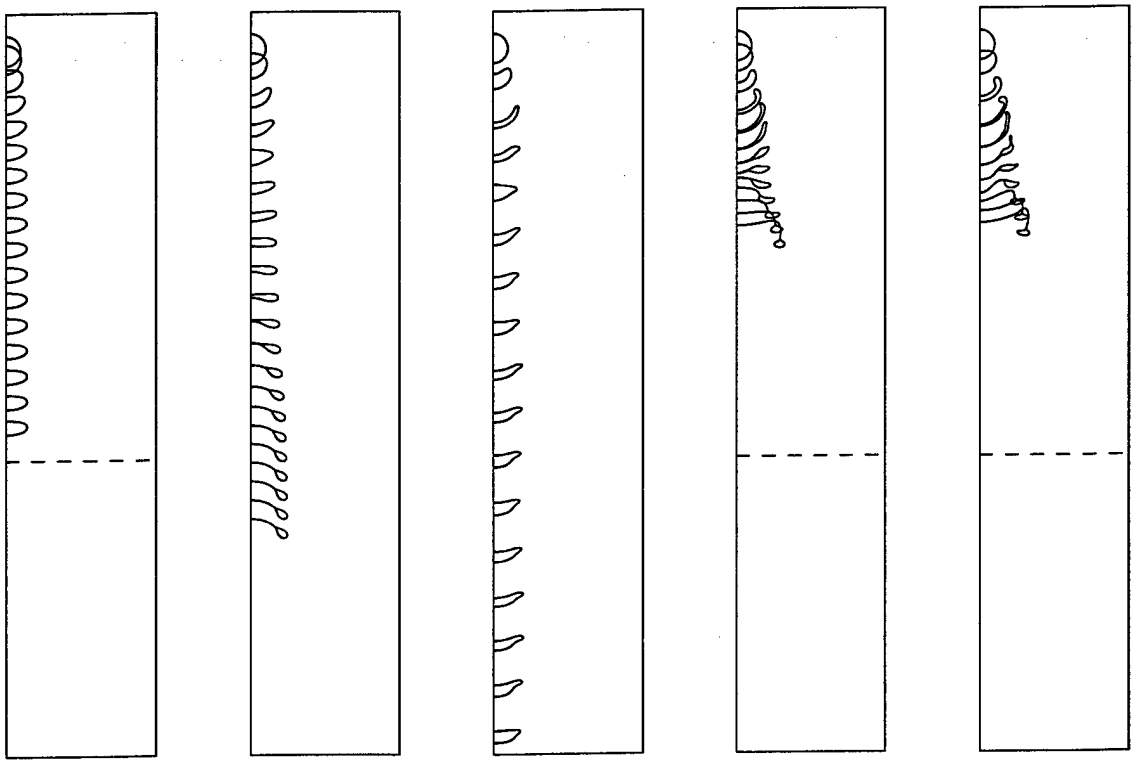

(a) $Eo = 12$ (b) $Eo = 24$ (c) $Eo = 48$ (d) $Eo = 96$ (e) $Eo = 144$

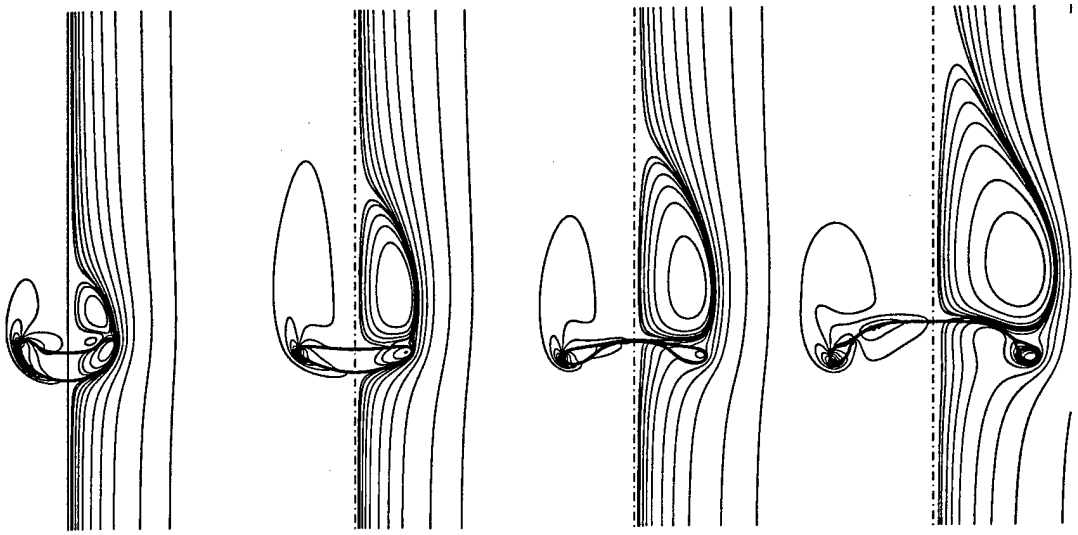

(a) $t^* = 4.24$ (b) $t^* = 8.48$ (c) $t^* = 12.7$ (d) $t^* = 17.0$

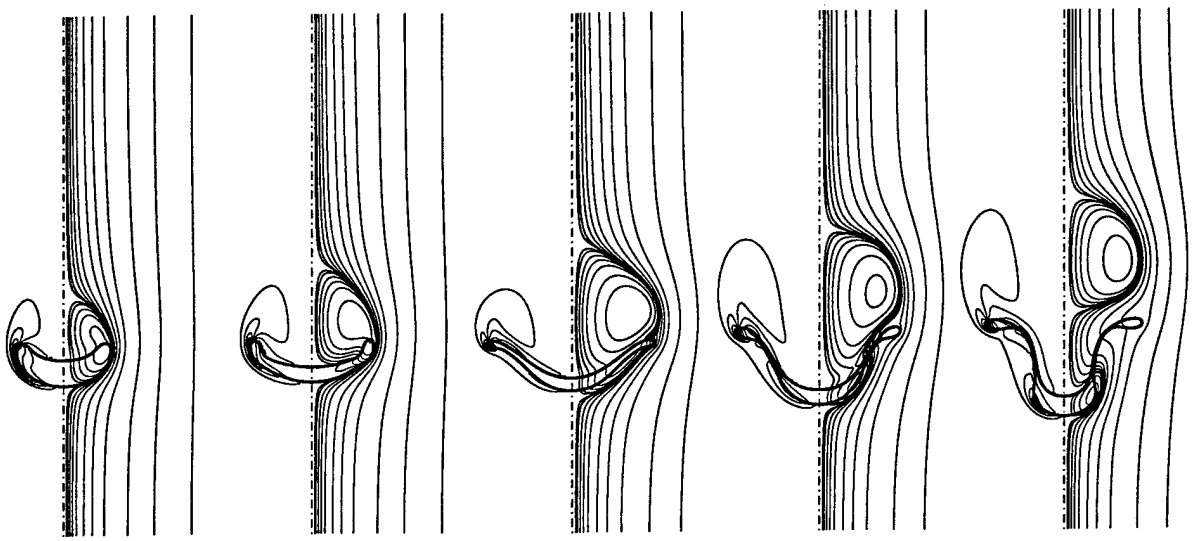

(a) $t^* = 3.06$ (b) $t^* = 4.08$ (c) $t^* = 5.10$ (d) $t^* = 6.12$ (e) $t^* = 7.14$

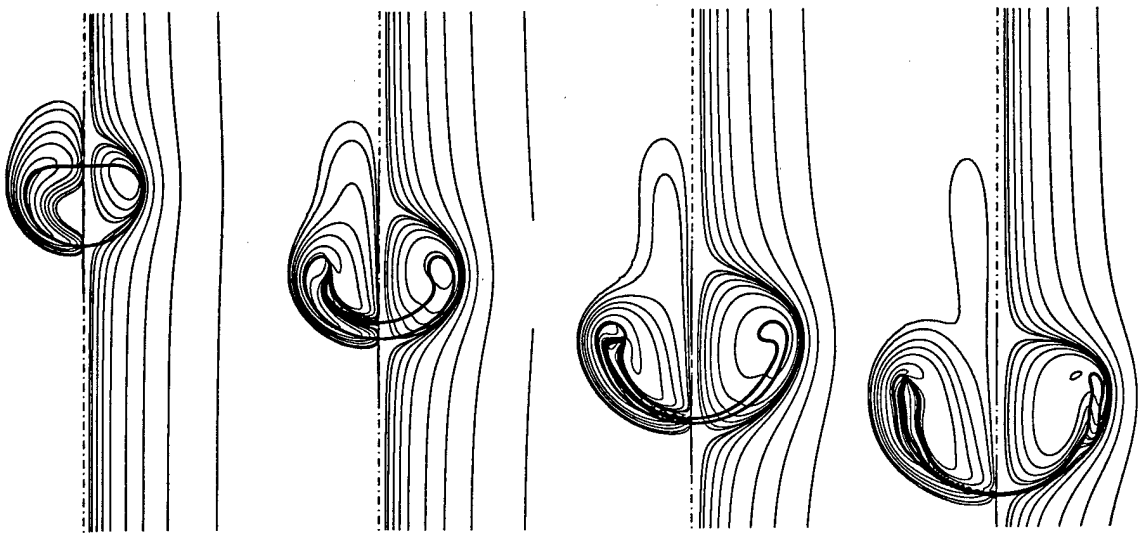

(a) $t^* = 3.87$ (b) $t^* = 7.75$ (c) $t^* = 11.6$ (d) $t^* = 15.5$

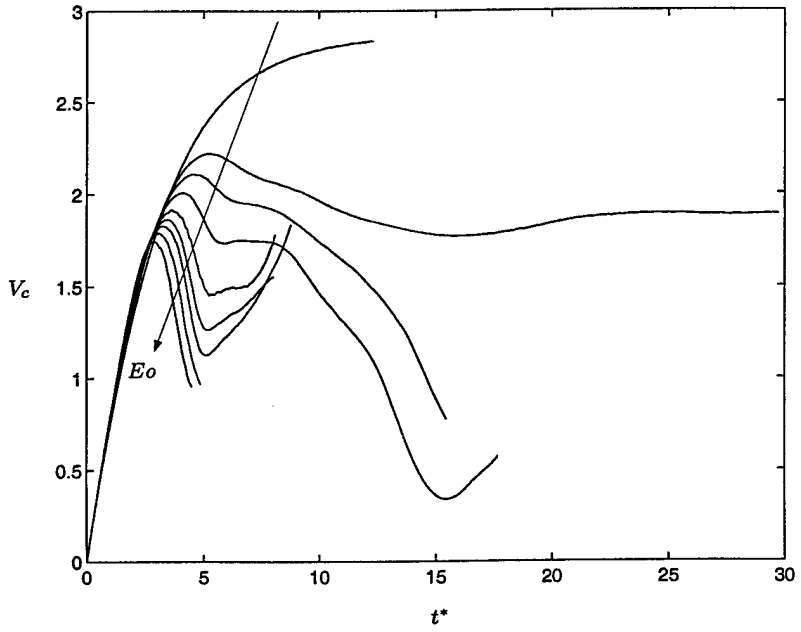
3
2.5
2
1.5
1
0.5
0
V_c
Eo
0
5
10
15
20
25
30
t^*

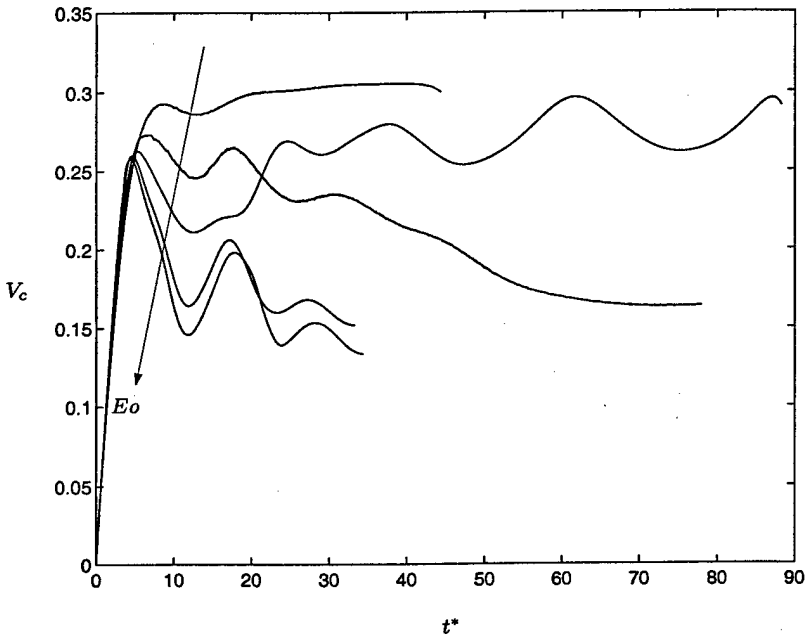
0.35
0.3
0.25
0.2
0.15
0.1
0.05
0
V_c
Eo
0
10
20
30
40
50
60
70
80
90
t^*

Figure 12

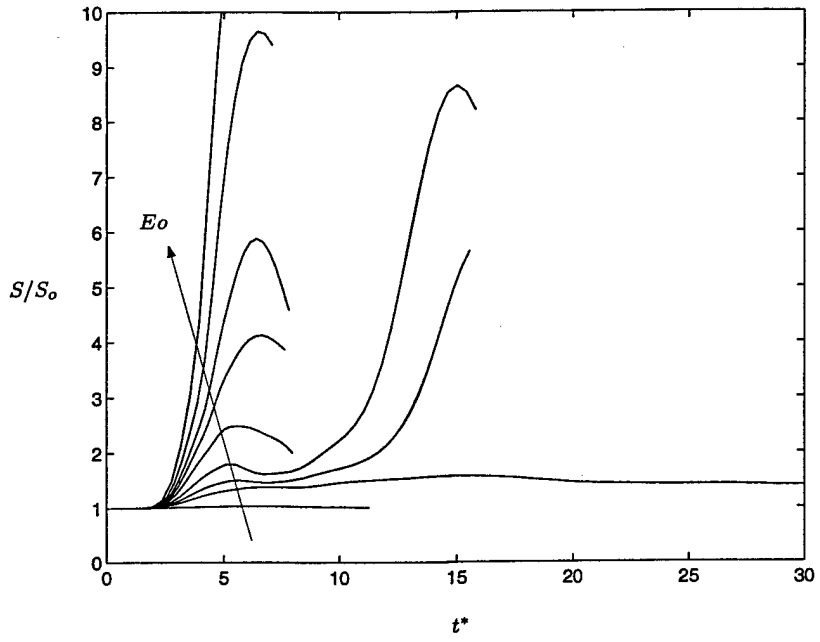

Figure 13

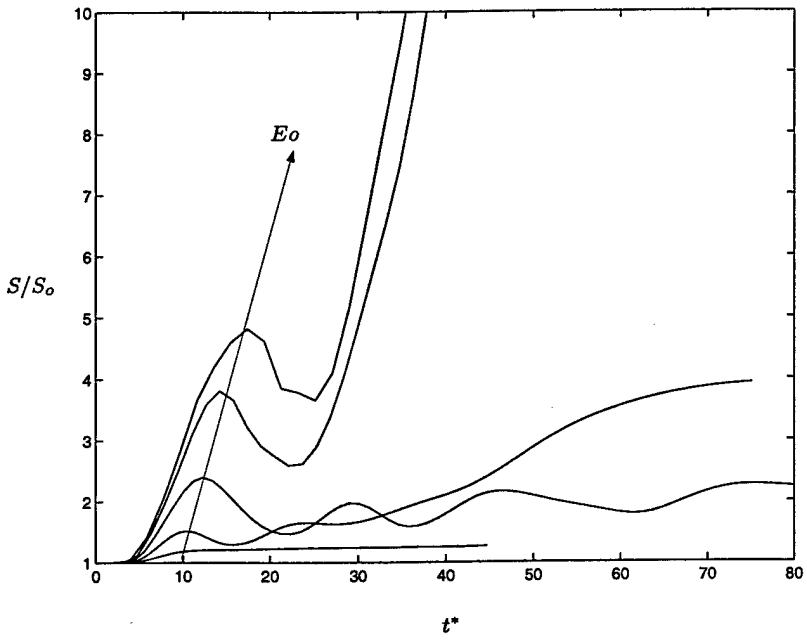

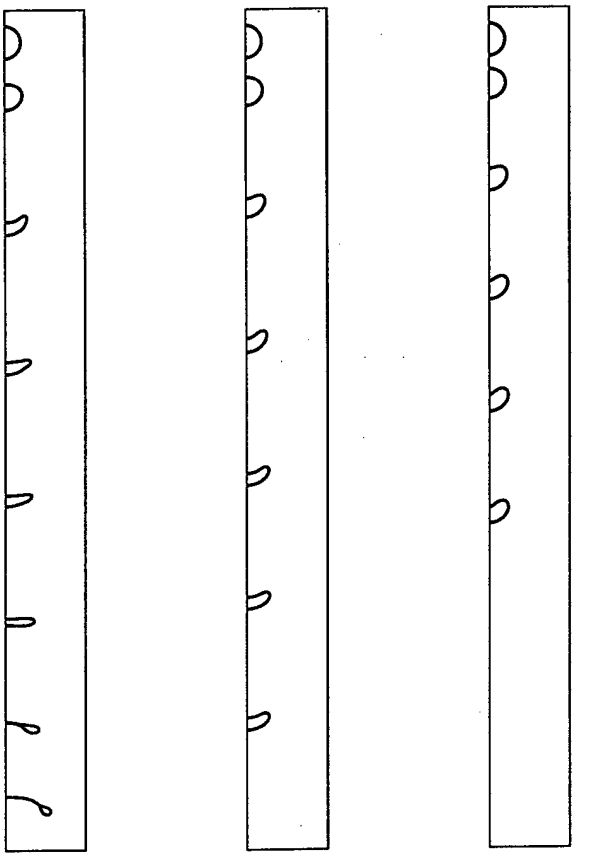

(a) $Oh = 0.05$ (b) $Oh = 0.125$ (c) $Oh = 0.25$

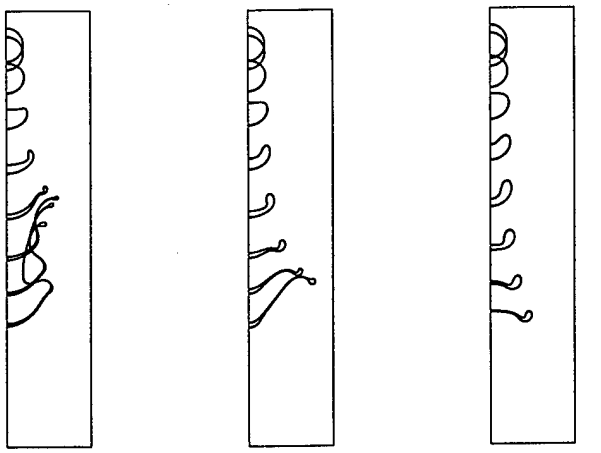

(d) $Oh = 0.05$ (e) $Oh = 0.125$ (f) $Oh = 0.25$

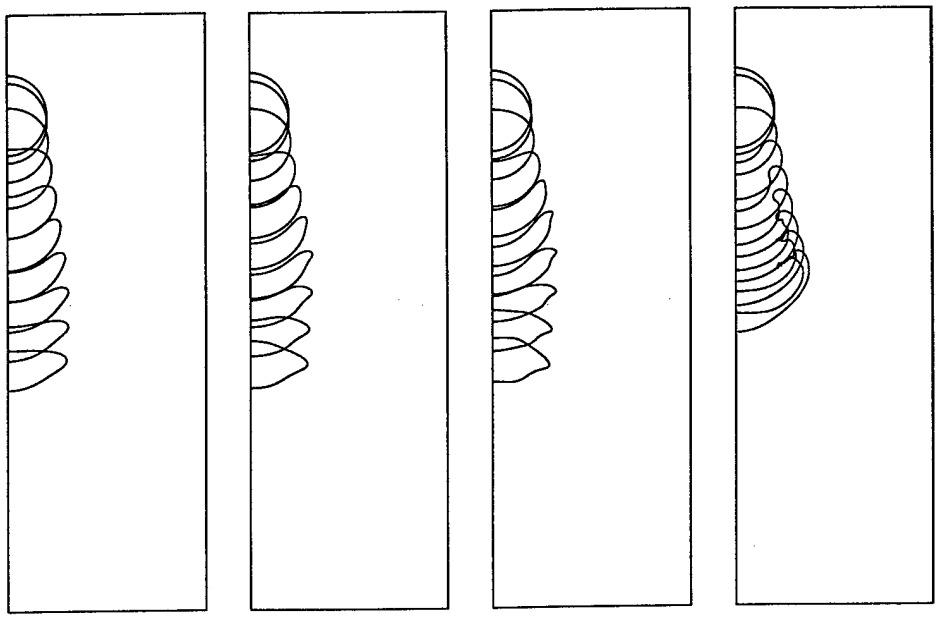

(a) $Oh_o = 0.05$ (b) $Oh_o = 0.025$ (c) $Oh_o = 0.01$ (d) Inviscid

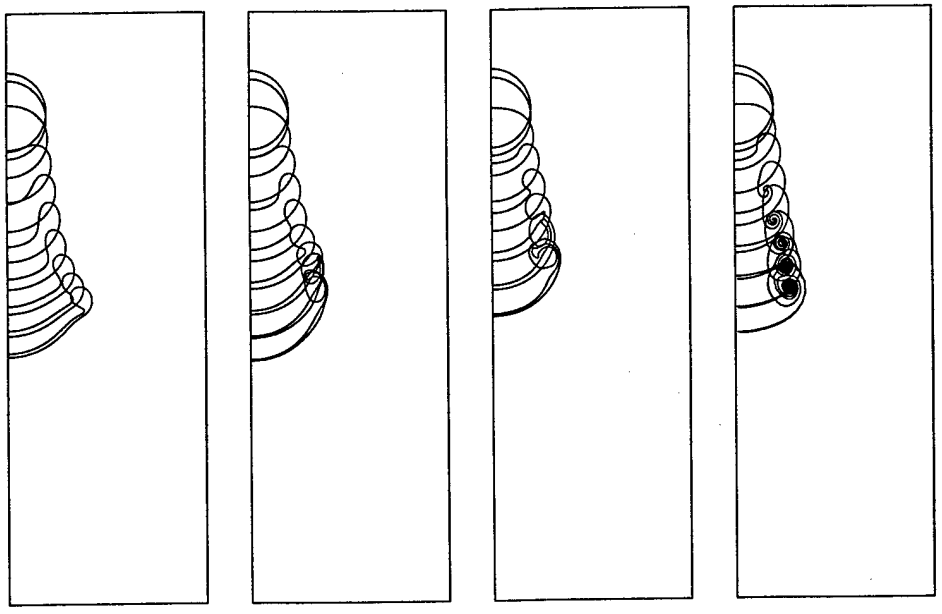

(e) $\hat{\mu} = 0.01021$ (f) $\hat{\mu} = 0.00513$ (g) $\hat{\mu} = 0.00204$ (h) Inviscid

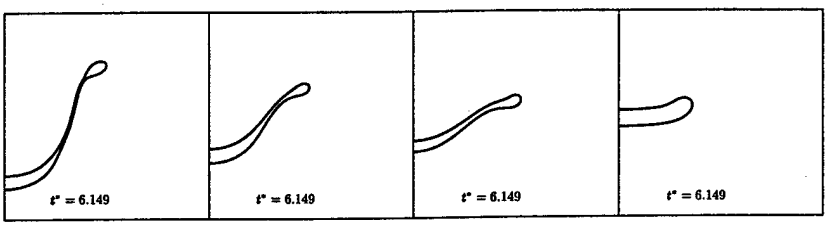

(a) $\rho_d/\rho_o = 10, Oh_o = 0.05, Eo = 72$

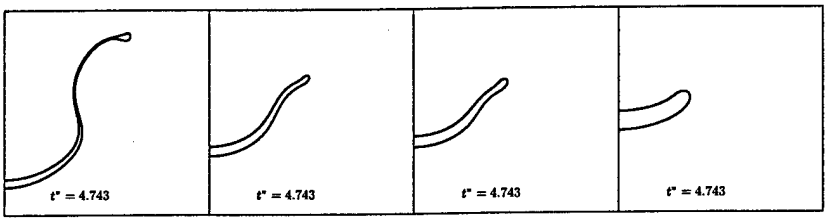

(b) $\rho_d/\rho_o = 10, Oh_o = 0.05, Eo = 144$

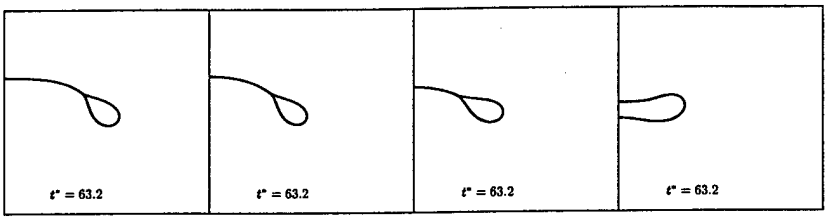

(c) $\rho_d/\rho_o = 1.15, Oh_o = 0.05, Eo = 24$

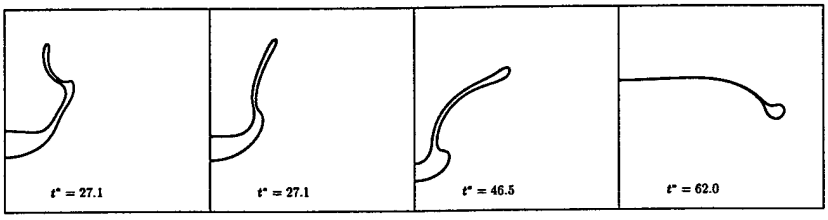

(d) $\rho_d/\rho_o = 1.15, Oh_o = 0.25, Eo = 144$

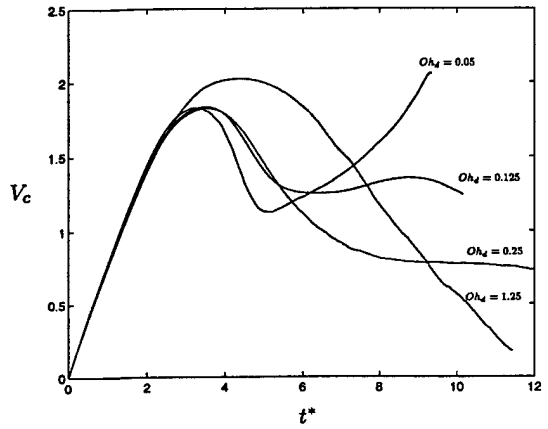

(a) $\rho_d/\rho_o = 10, Oh_o = 0.05, Eo = 72$

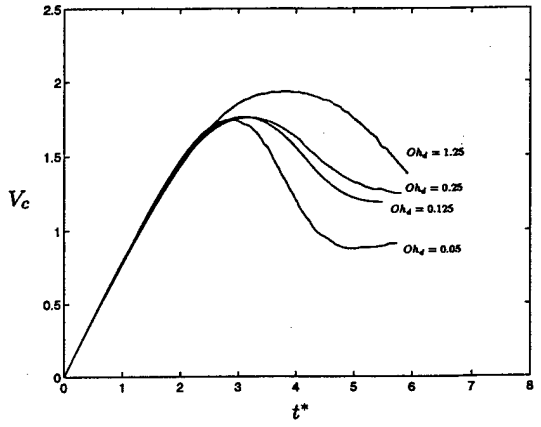

(b) $\rho_d/\rho_o = 10, Oh_o = 0.05, Eo = 144$

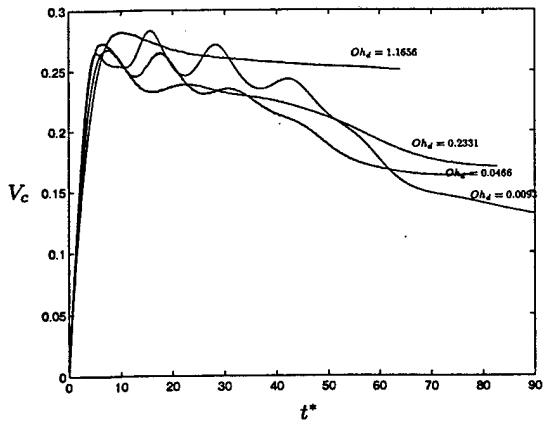

(c) $\rho_d/\rho_o = 1.15, Oh_o = 0.05, Eo = 24$

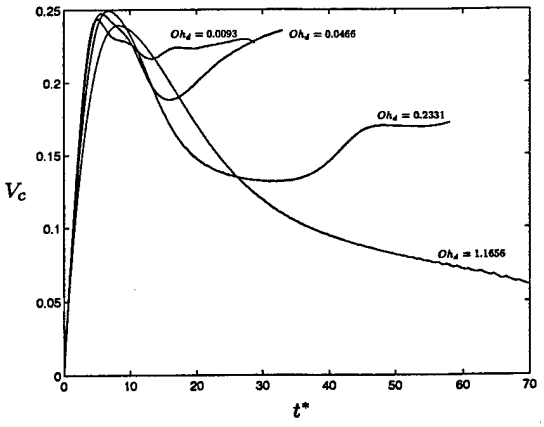

(d) $\rho_d/\rho_o = 1.15, Oh_o = 0.25, Eo = 144$

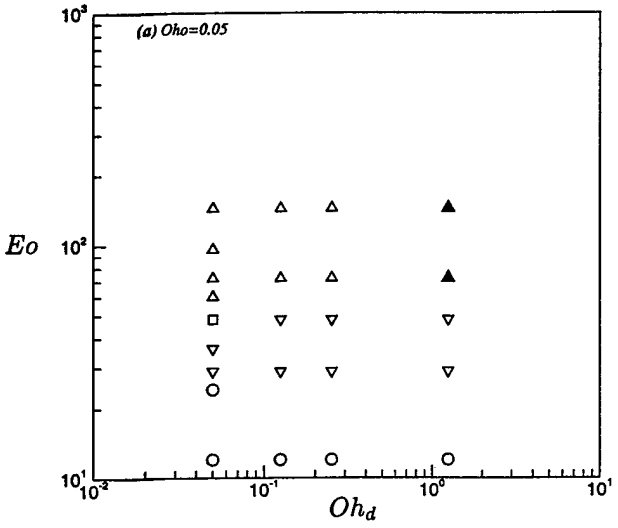
(a) Oho=0.05
Eo
Oh_d

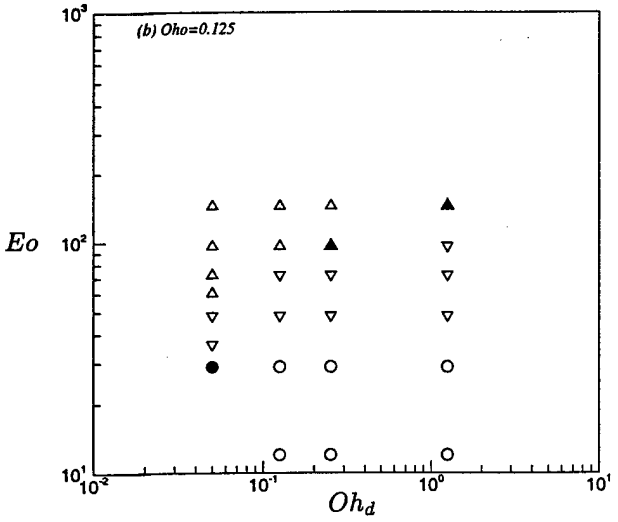
(b) Oho=0.125
Eo
Oh_d

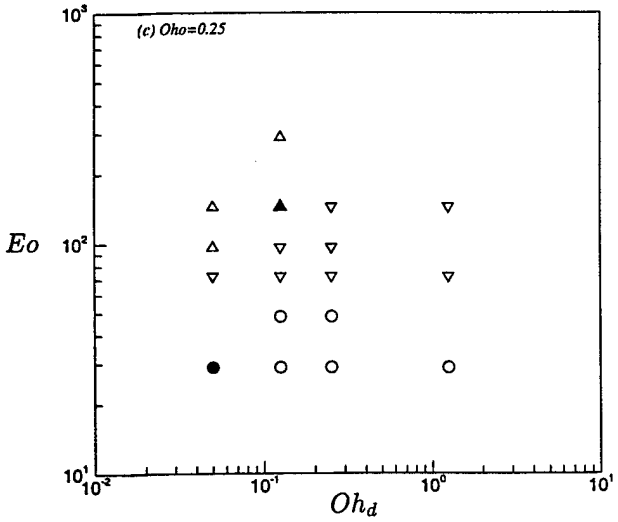
(c) Oho=0.25
Eo
Oh_d

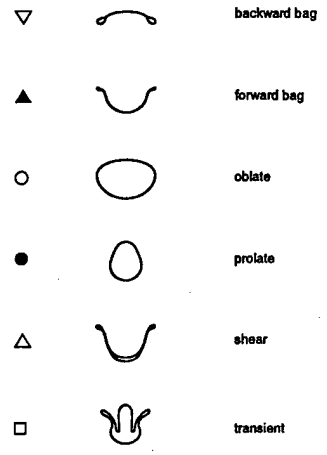
backward bag
forward bag
oblate
prolate
shear
transient

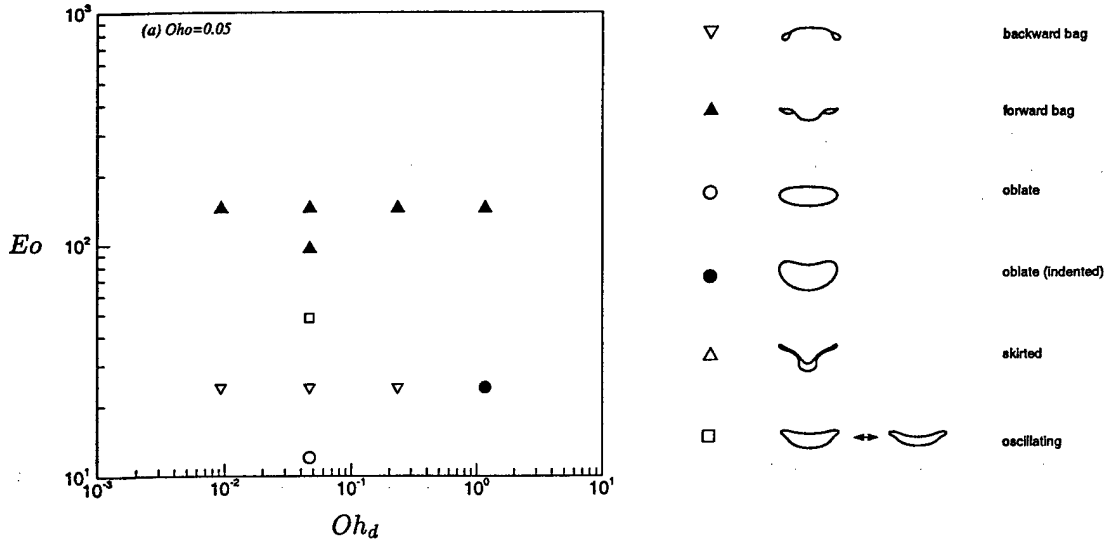
(a) Oho=0.05
Eo
Oh_d
backward bag
forward bag
oblate
oblate (indented)
skirted
oscillating

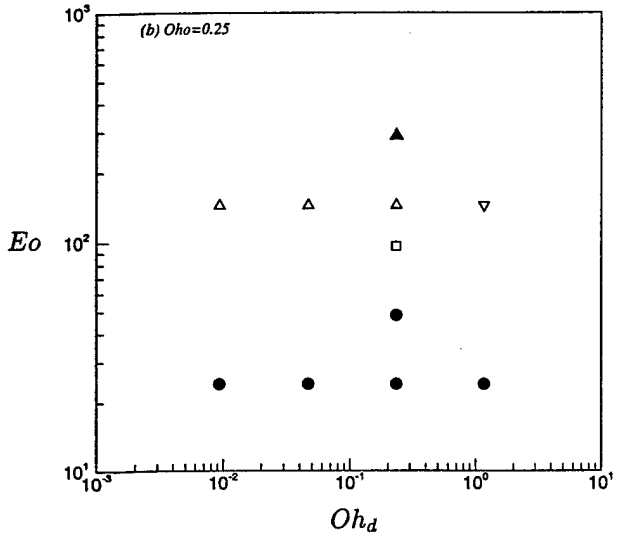
(b) Oho=0.25
Eo
Oh_d

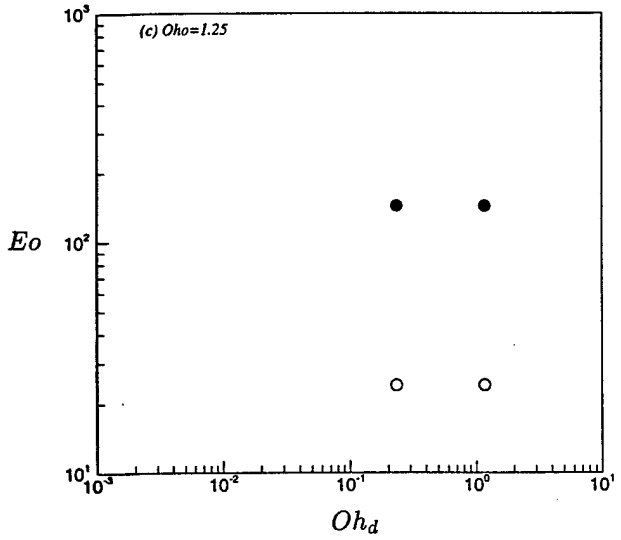
(c) Oho=1.25
Eo
Oh_d

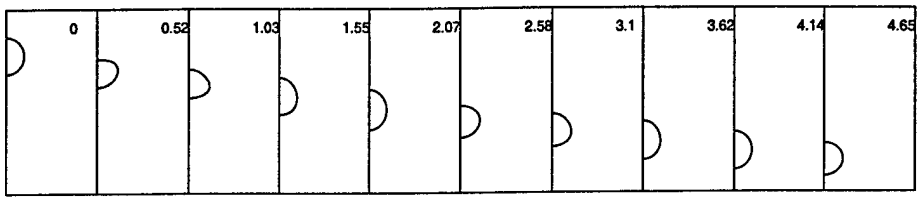

(a) $We = 2.73$

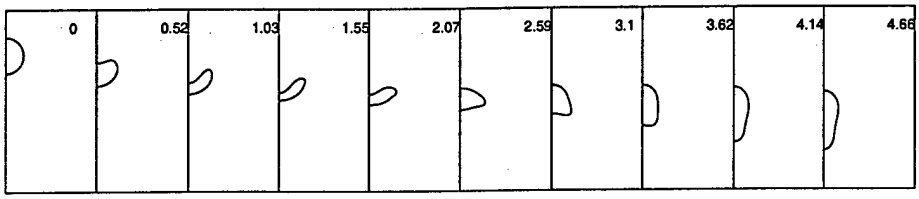

(b) $We = 13.7$

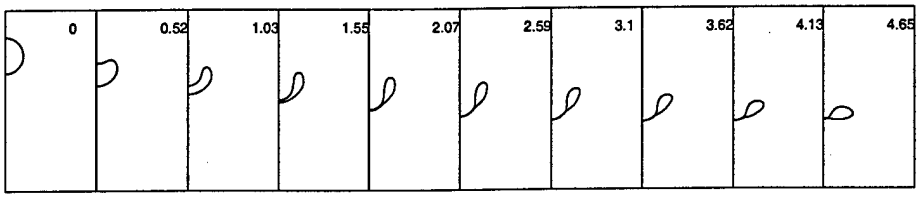

(c) $We = 27.4$

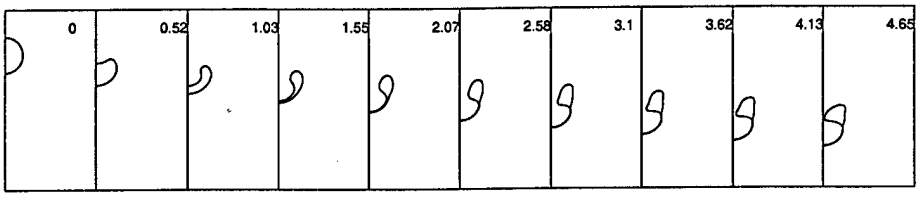

(d) $We = 54.7$

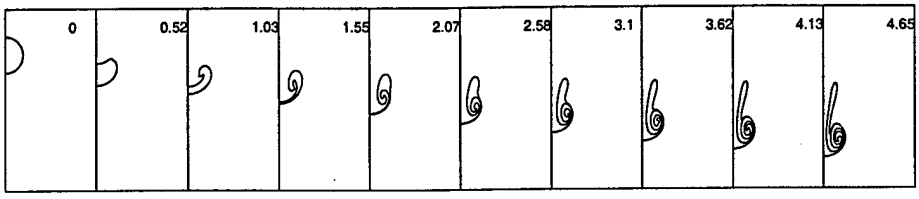

(e) $We = \infty$

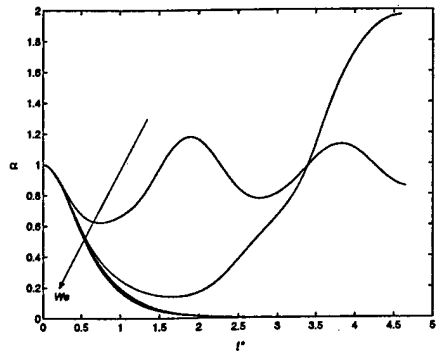

(a) aspect ratio

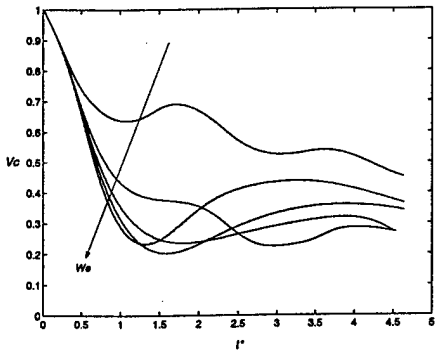

(b) centroid velocity

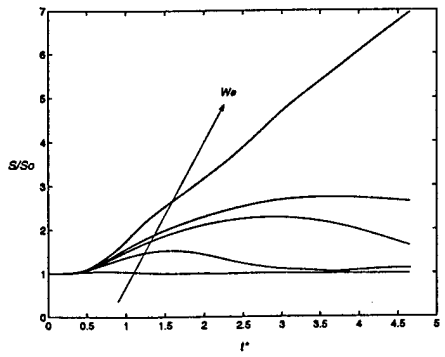

(c) surface area

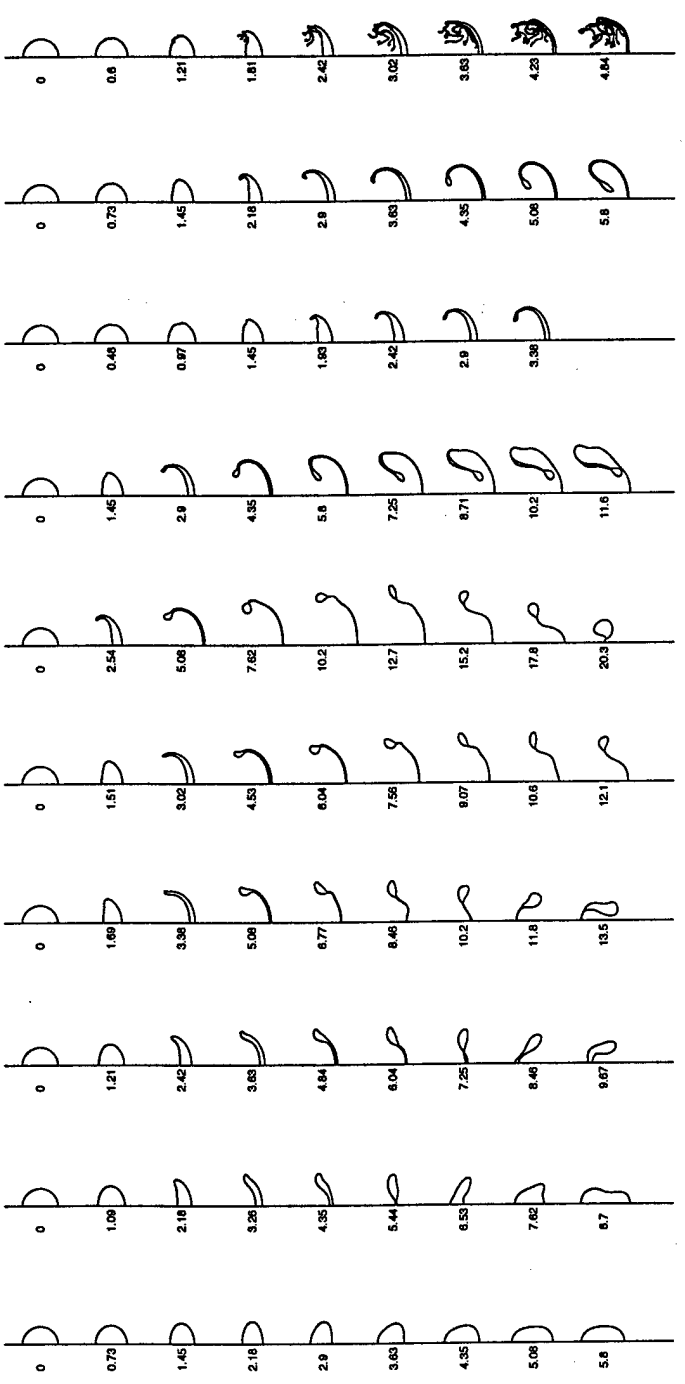

(a) $We = 3.74$ (b) $We = 12.5$ (c) $We = 18.7$ (d) $We = 28.1$ (e) $We = 37.4$ (f) $We = 46.8$ (g) $We = 56.1$ (h) $We = 74.8$ (i) $We = 93.5$ (j) $We = \infty$

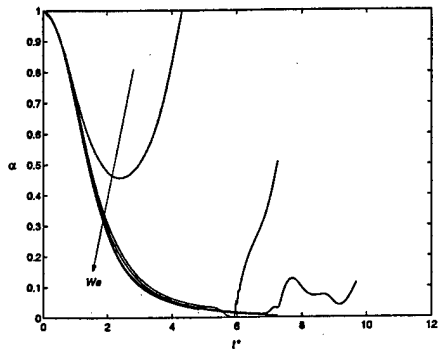

(a) aspect ratio

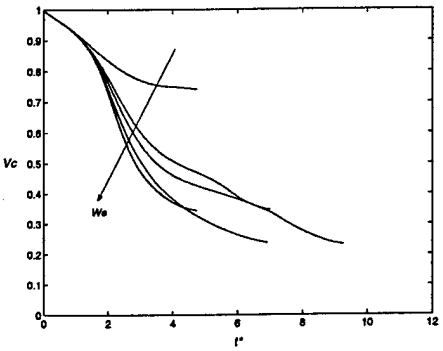

(b) centroid velocity

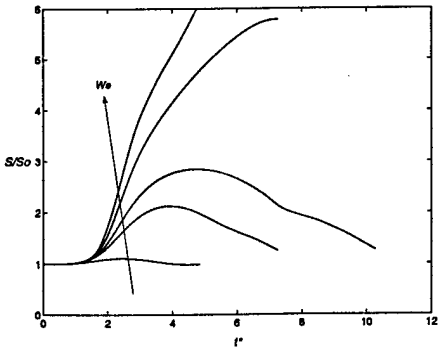

(c) surface area

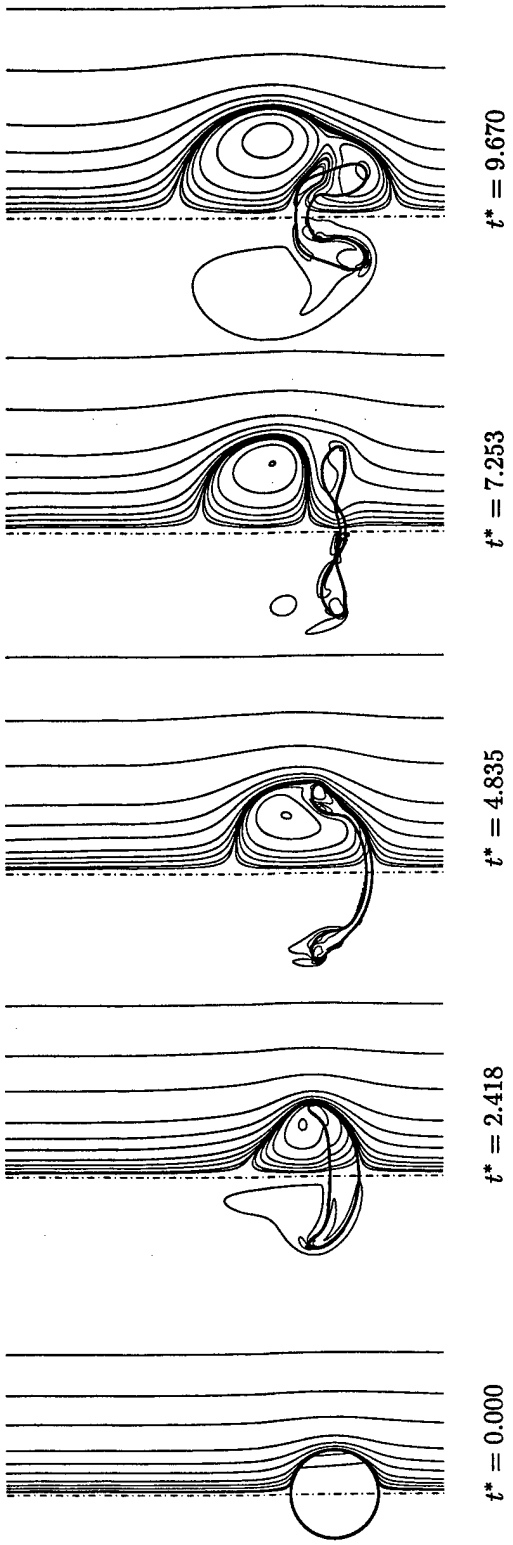
$t^* = 9.670$
$t^* = 7.253$
$t^* = 4.835$
$t^* = 2.418$
$t^* = 0.000$

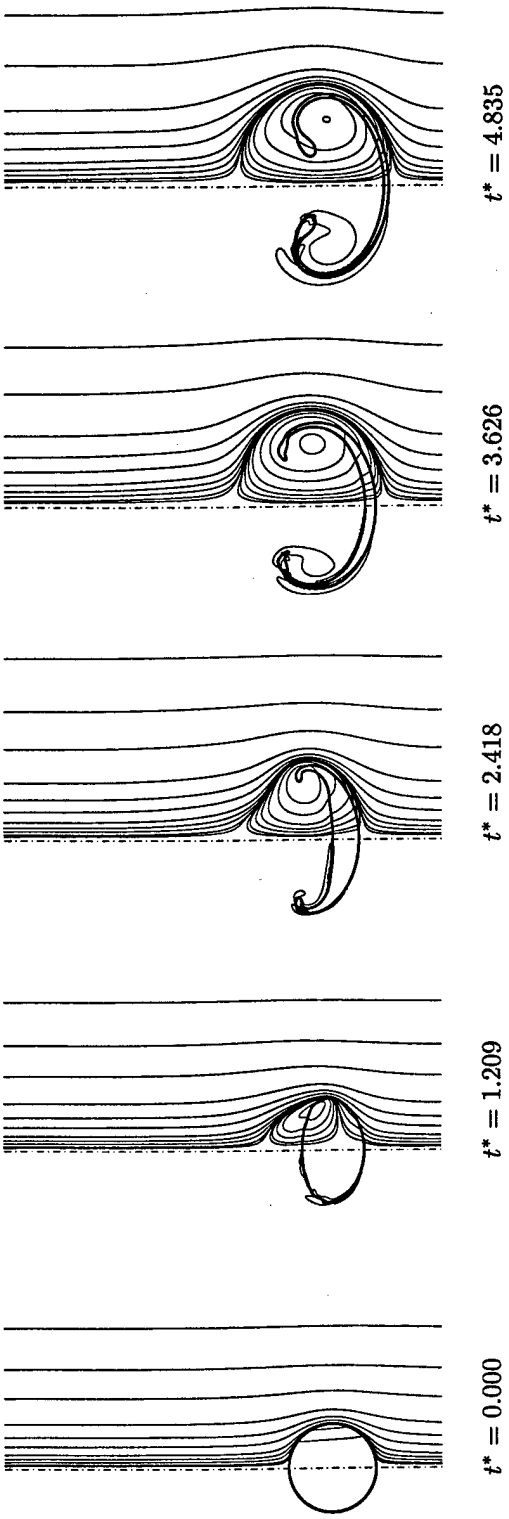
$t^* = 4.835$
$t^* = 3.626$
$t^* = 2.418$
$t^* = 1.209$
$t^* = 0.000$

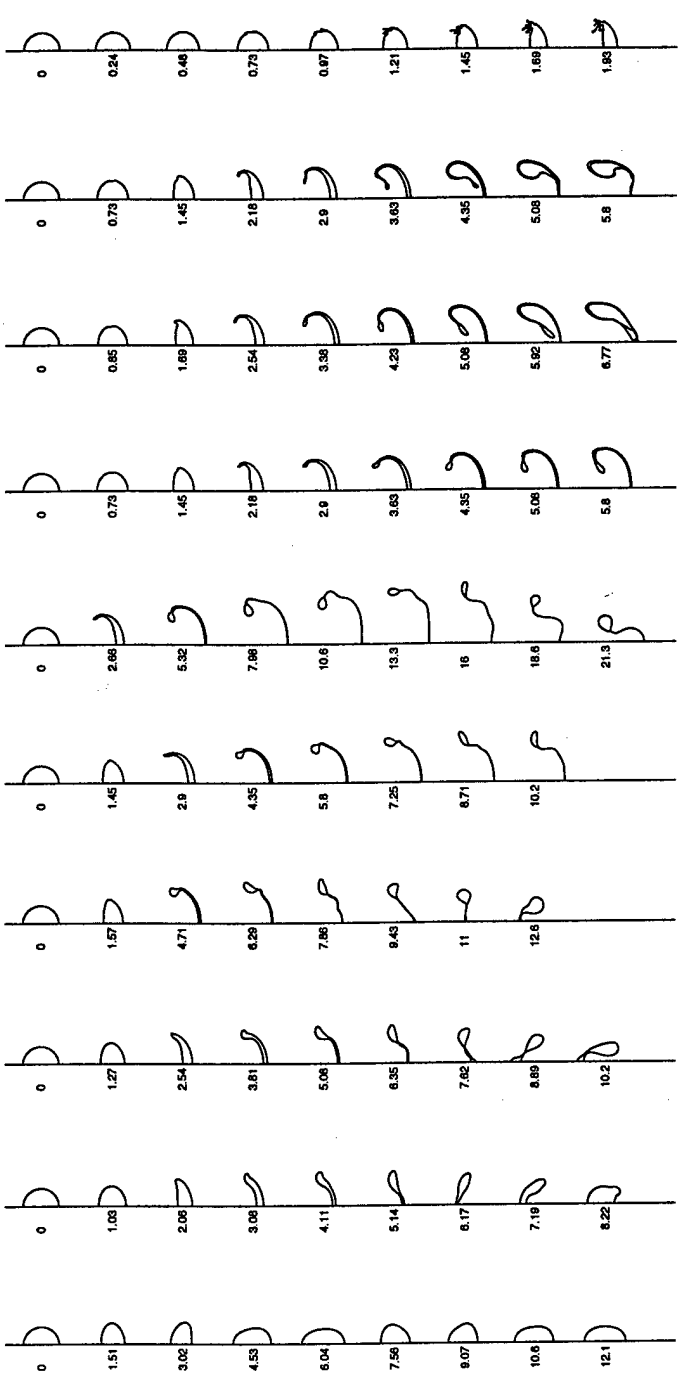

(a) $We = 3.74$ (b) $We = 12.5$ (c) $We = 18.7$ (d) $We = 28.1$ (e) $We = 37.4$ (f) $We = 46.8$ (g) $We = 56.1$ (h) $We = 74.8$ (i) $We = 93.5$ (j) $We = \infty$

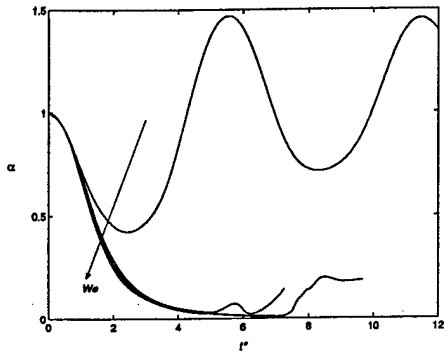

(a) aspect ratio

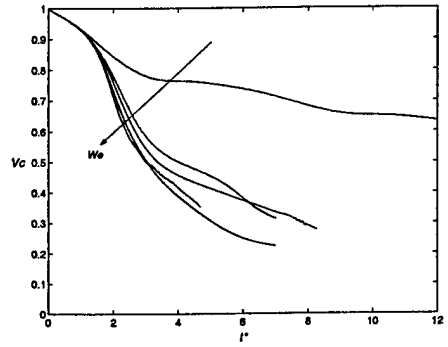

(b) centroid velocity

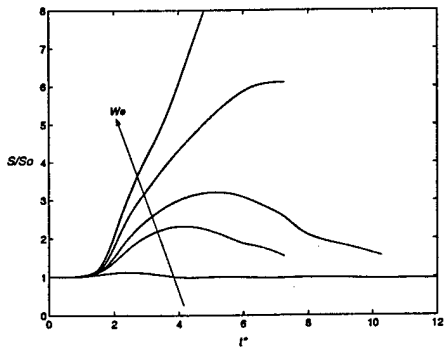

(c) surface area

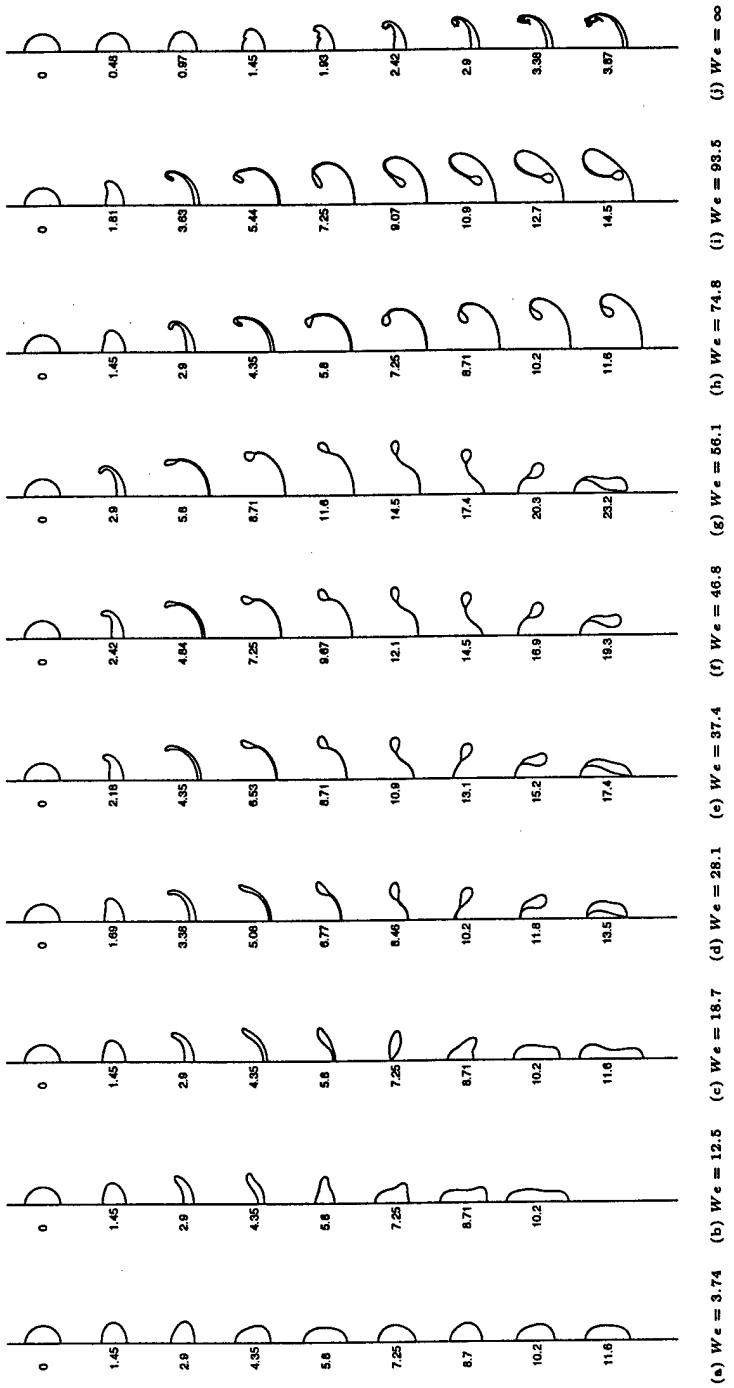

(a) $We = 3.74$ (b) $We = 12.5$ (c) $We = 18.7$ (d) $We = 28.1$ (e) $We = 37.4$ (f) $We = 46.8$ (g) $We = 56.1$ (h) $We = 74.8$ (i) $We = 93.5$ (j) $We = \infty$

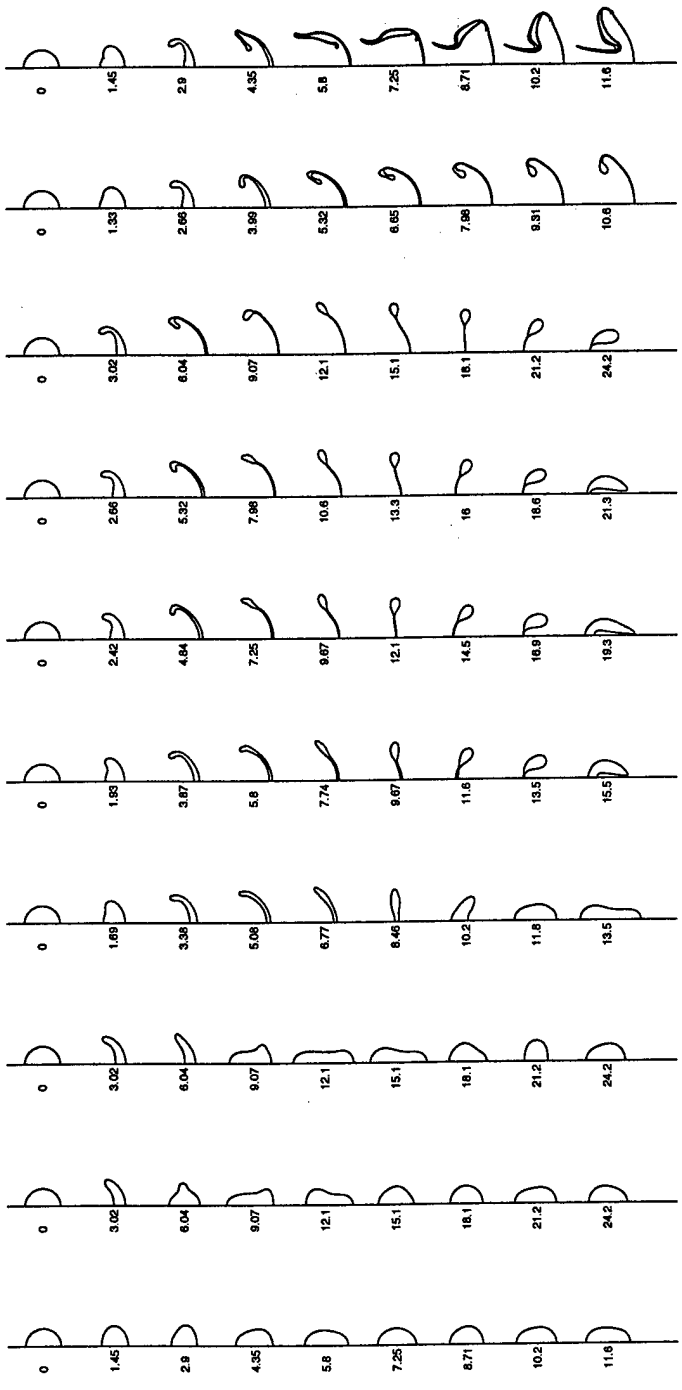

(a) $We = 3.74$ (b) $We = 12.5$ (c) $We = 18.7$ (d) $We = 28.1$ (e) $We = 37.4$ (f) $We = 46.8$ (g) $We = 56.1$ (h) $We = 74.8$ (i) $We = 93.5$ (j) $We = \infty$

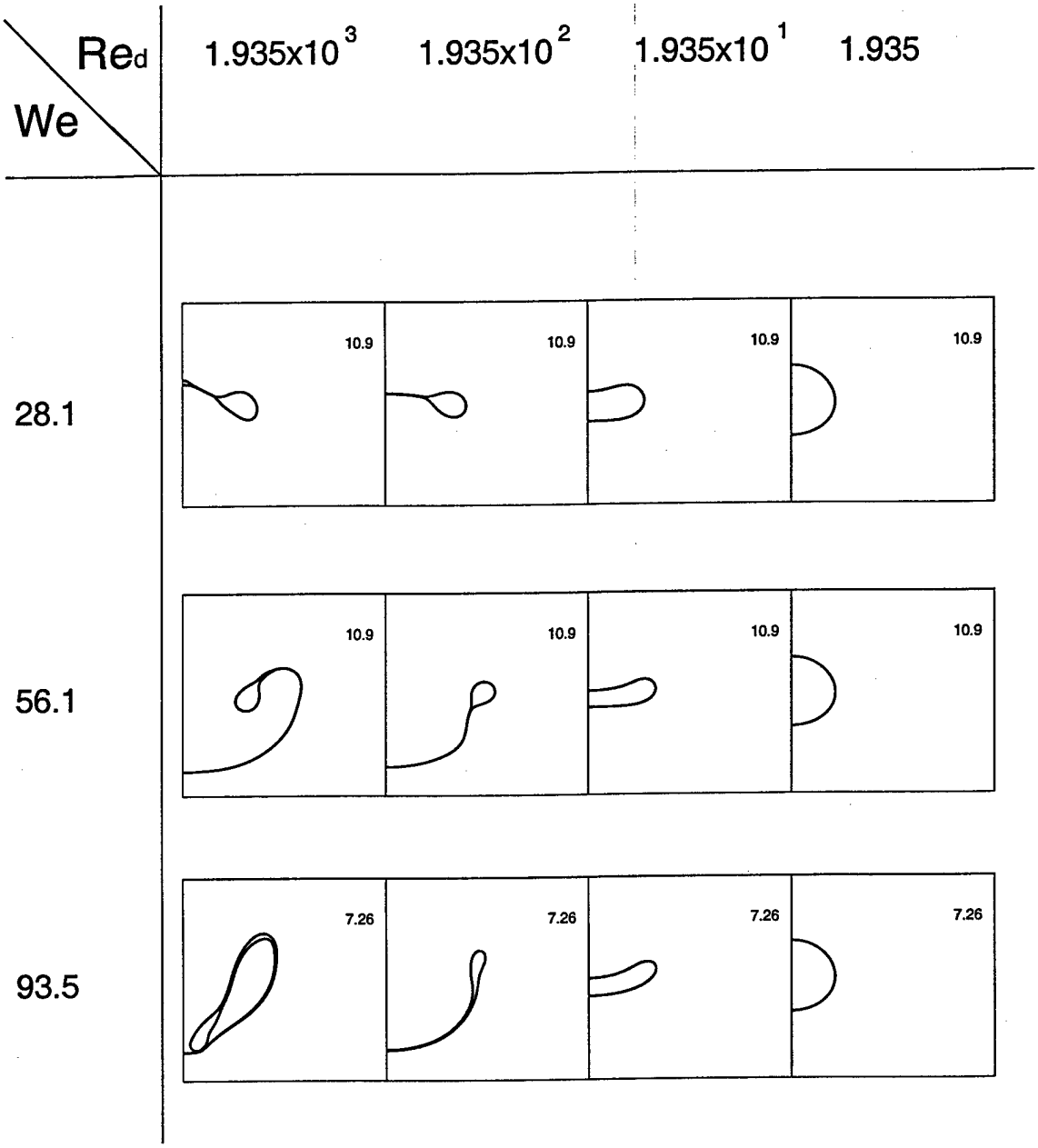
Re_d
We
1.935x10^3
1.935x10^2
1.935x10^1
1.935
28.1
56.1
93.5
10.9
10.9
10.9
10.9
10.9
10.9
10.9
10.9
7.26
7.26
7.26
7.26

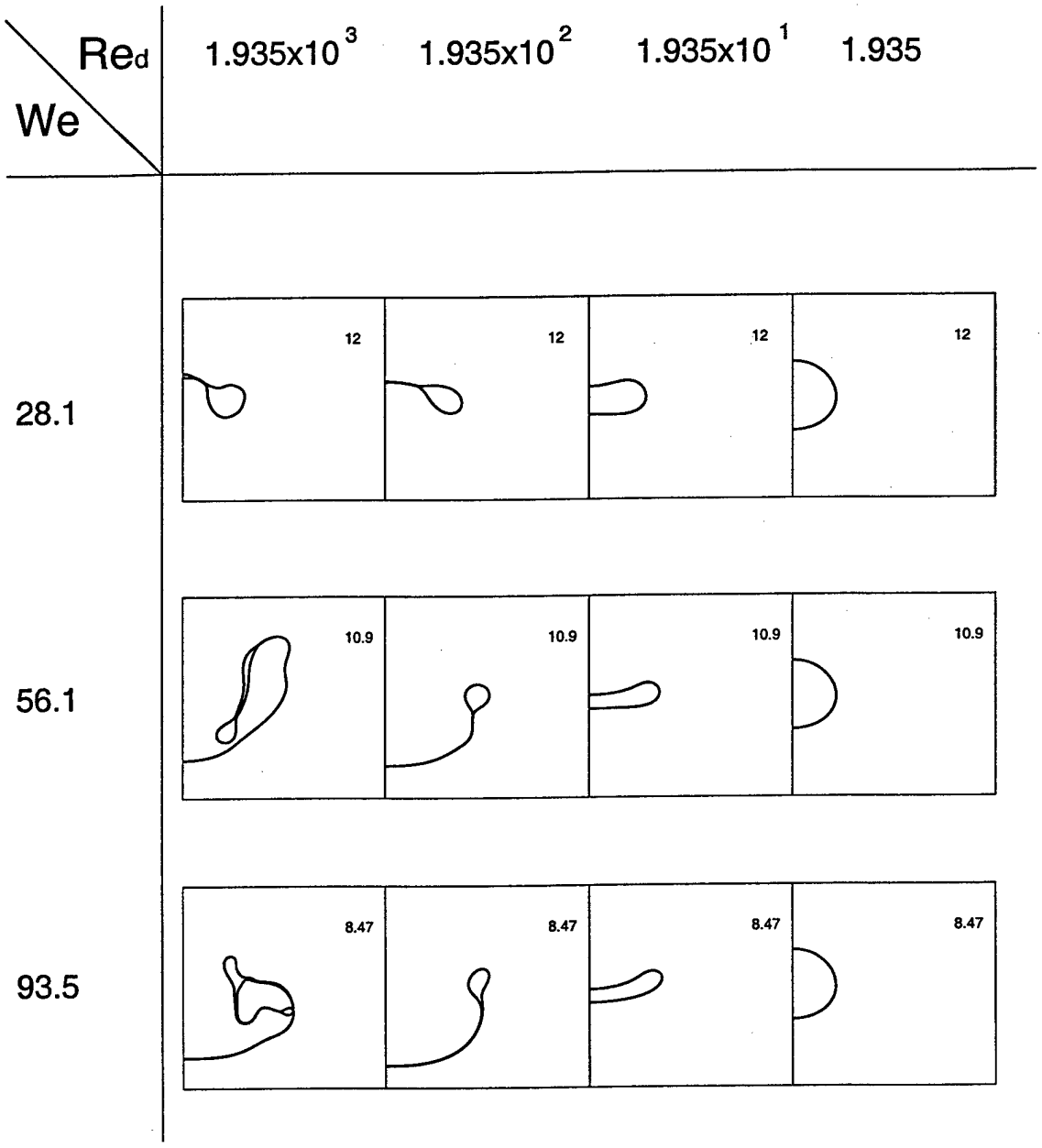
Red
We
1.935x10^3
1.935x10^2
1.935x10^1
1.935
28.1
56.1
93.5
12
12
12
12
10.9
10.9
10.9
10.9
8.47
8.47
8.47
8.47

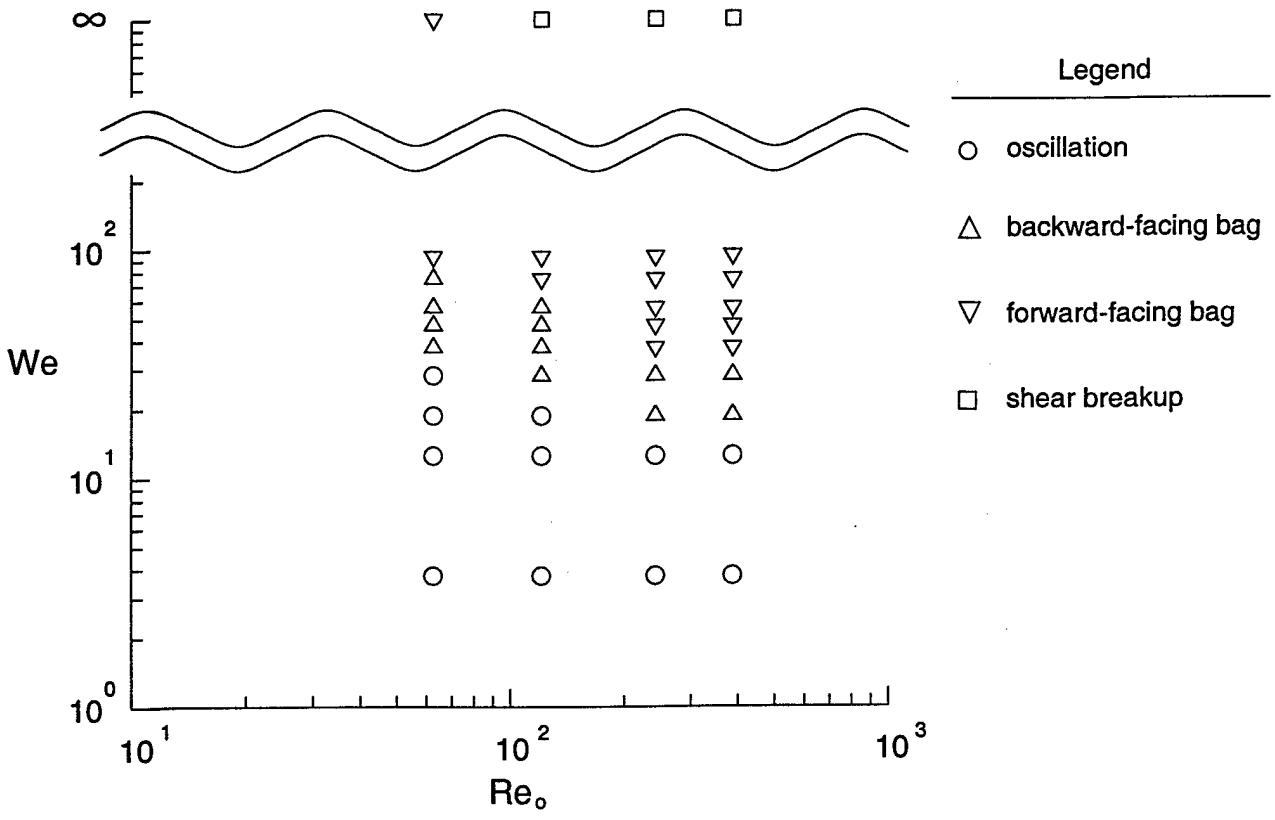
∞
10^2
10^1
10^0
We
10^1
10^2
10^3
Re_o
Legend
oscillation
backward-facing bag
forward-facing bag
shear breakup

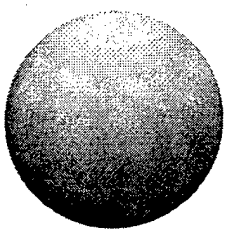

(a) $t = 0.25$

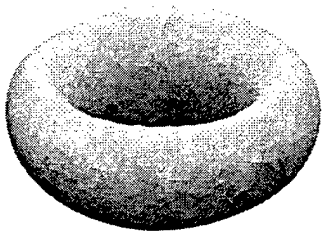

(b) $t = 7.75$

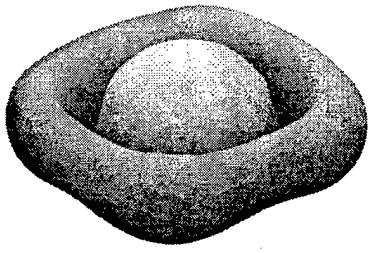

(c) $t = 15.5$

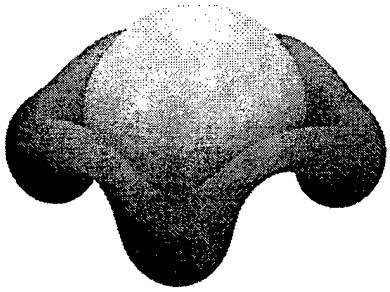

(d) $t = 20.0$

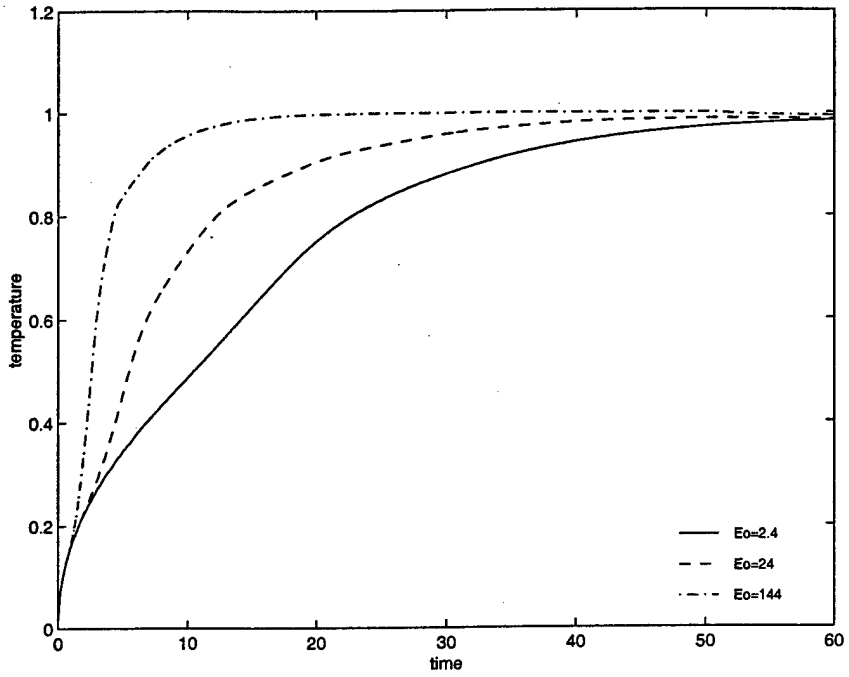
temperature
time
Eo=2.4
Eo=24
Eo=144

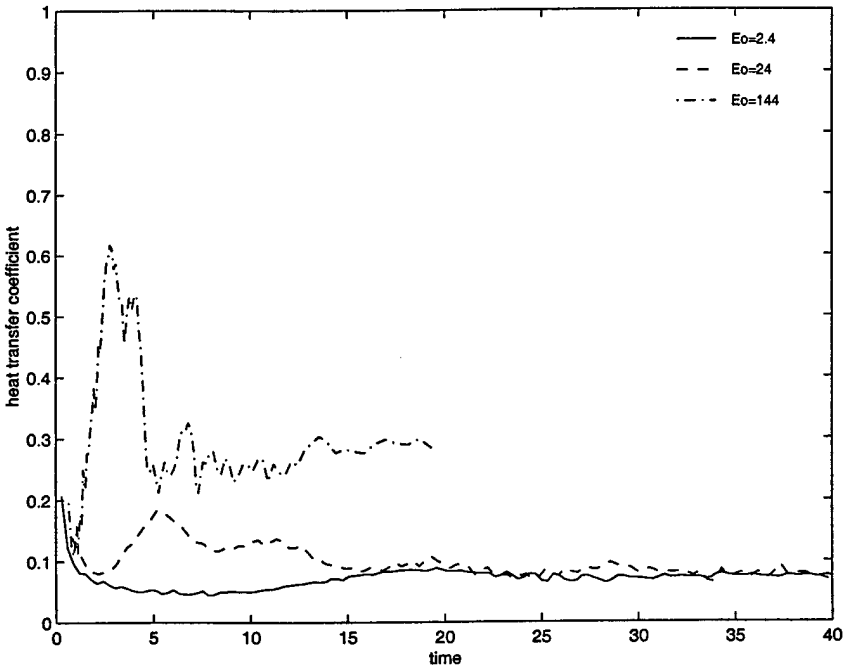
heat transfer coefficient
time
Eo=2.4
Eo=24
Eo=144

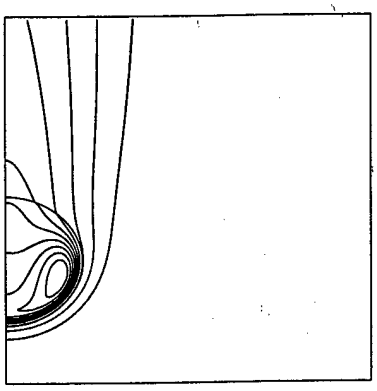

(a) $Eo = 2.4$

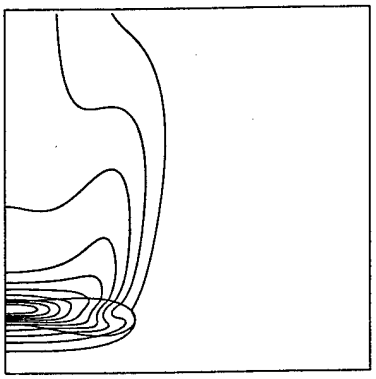

(b) $Eo = 24$

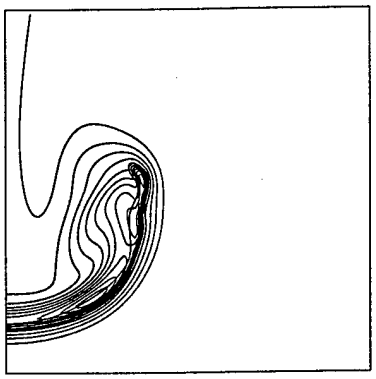

(c) $Eo = 144$

REFERENCES

[1] D. A. Drew and S. L. Passman, *Theory of Multicomponent Fluids* (Springer-Verlag, 1998), pp. 135–233.

[2] C. Crowe, M. Sommerfeld, and Y. Tsuji, *Multiphase Flows with Droplets and Particles* (CRC Press, 1997), pp. 191–284.

[3] R. D. Reitz and R. Diwakar, "Effect of Drop Breakup on Fuel Sprays," SAE Paper 860469 (1986).

[4] P. J. O'Rourke and A. A. Amsden, "The TAB Method for Numerical Calculation of Spray Droplet Breakup," SAE Paper 872089 (1987).

[5] A. B. Liu, D. Mather, and R. D. Reitz, "Modeling the Effects of Drop Drag and Breakup on Fuel Sprays," SAE Paper 930072 (1993).

[6] A. B. Liu and R. D. Reitz, "Mechanics of Air-Assisted Liquid Atomization," Atomization and Sprays **3**, 55 (1993).

[7] Y. M. Kim and T. S. Wang, "Numerical Studies on Droplet Breakup Models," J. Propulsion **11**, 389 (1994).

[8] S.-C. Kong, Z. Han, and R. D. Reitz, "The Development and Application of a Diesel Ignition and Combustion Model for Multidimensional Engine Simulation," SAE Paper 950278 (1995).

[9] G. I. Taylor, "The Shape and Acceleration of a Drop in a High-Speed Air Stream," in *The Scientific Papers by G. I. Taylor*, edited by G. K. Batchelor (Cambridge University Press, 1963), Vol. 3, pp. 457–464.

[10] W. R. Lane, "Shatter of Drops in Streams of Air," Industrial and Engineering Chemistry **43**, 1312 (1951).

[11] J. O. Hinze, "Fundamentals of the Hydrodynamic Mechanism of Splitting in Dispersion Process," A.I.Ch.E. Journal **1**, 289 (1955).

[12] F. C. Haas, "Stability of Droplets Suddenly Exposed to a High Velocity Gas Stream," A.I.Ch.E. Journal **10**, 920 (1964).

[13] A. R. Hanson, E. G. Domich, and H. S. Adams, "Shock Tube Investigation of the Breakup of Drops by Air Blasts," Phys. Fluids **6**, 1070 (1964).

[14] A. A. Ranger and J. A. Nicholls, "Aerodynamic Shattering of Liquid Drops," AIAA Journal **7**, 285 (1969).

[15] B. E. Gel'fand, S. A. Gubin, S. M. Kogarko, and S. P. Komar, "Singularities of the Breakup of Viscous Liquid Droplets in Shock Waves," J. Eng. Phys. **25**, 1140 (1973).

[16] A. A. Borisov, B. E. Gel'fand, M. S. Natanzon, and O. M. Kossov, "Droplet Breakup Regimes and Criteria for Their Existence," J. Eng. Phys. **40**, 44 (1981).

[17] S. A. Krzeczkowski, "Measurement of Liquid Droplet Disintegration Mechanisms," Int. J. Multiphase Flow **6**, 227 (1980).

[18] M. Pilch and C. A. Erdman, "Use of Breakup Time Data and Velocity History Data to Predict the Maximum Size of Stable Fragments for Acceleration-Induced Breakup of a Liquid Drop," Int. J. Multiphase Flow **13**, 741 (1987).

[19] A. Wierzba, "Deformation and Breakup of Liquid Drops in a Gas Stream at Nearly Critical Weber Numbers," Experiments in Fluids **9**, 59 (1990).

[20] R. H. Magarvey and B. W. Taylor, "Free Fall Breakup of Large Drops," J. Appl. Phys. **27**, 1129 (1956).

[21] L.-P. Hsiang and G. M. Faeth, "Near-Limit Drop Deformation and Secondary Breakup," Int. J. Multiphase Flow **18**, 635 (1992).

[22] L.-P. Hsiang and G. M. Faeth, "Drop Properties after Secondary Breakup," Int. J. Multiphase Flow **19**, 721 (1993).

[23] L.-P. Hsiang and G. M. Faeth, "Drop Deformation and Breakup due to Shock Wave and Steady

Disturbances," Int. J. Multiphase Flow **21**, 545 (1995).

[24] D. D. Joseph, J. Belanger, and G. S. Beavers, "Breakup of a Liquid Drop Suddenly Exposed to a High-Speed Airstream," (submitted for publication).

[25] R. Clift, J. R. Grace and M. E. Weber, *Bubbles, Drops, and Particles* (Academic Press, 1978), p. 346.

[26] A. H. Lefebvre, *Atomization and Sprays* (Taylor and Francis, 1989), pp. 29–34.

[27] L. Bayvel and Z. Orzechowski, *Liquid Atomization* (Taylor and Francis, 1993), pp. 69–81.

[28] S. S. Sadhal, P. S. Ayyaswamy, and J. N. Chung, *Transport Phenomena with Drops and Bubbles* (Springer-Verlag, 1996), pp. 389–392.

[29] R. I. Nigmatulin, *Dynamics of Multiphase Media 1* (Hemisphere Publishing Corporation, 1991), pp. 150–163.

[30] M. Kojima, E. J. Hinch, and A. Acrivos, "The Formation and Expansion of a Toroidal Drop Moving in a Viscous Fluid," Phys. Fluids **27**, 19 (1984).

[31] C. J. Koh and L. G. Leal, "The Stability of Drop Shapes for Translation at Zero Reynolds Number through a Quiescent Fluid," Phys. Fluids A **1**, 1309 (1989).

[32] C. J. Koh and L. G. Leal, "An Experimental Investigation on the Stability of Viscous Drops Translating through a Quiescent Fluid," Phys. Fluids A **2**, 2103 (1990).

[33] C. Pozrikidis, "The Instability of a Moving Viscous Drop," J. Fluid Mech. **210**, 1 (1990).

[34] N. Baumann, D. D. Joseph, P. Mohr, and Y. Renardy, "Vortex Rings of One Fluid in Another in Free Fall," Phys. Fluids A **4**, 567 (1992).

[35] D. S. Dandy and L. G. Leal, "Buoyancy-Driven Motion of a Deformable Drop through a Quiescent Liquid at Intermediate Reynolds Numbers," J. Fluid Mech. **208**, 161 (1989).

[36] P. K. Volkov, "Steady Rise of a Liquid Drop in a Viscous Fluid," J. Appl. Mech. Tech. Phys. **33**,

71 (1992).

[37] L. A. Bozzi, J. Q. Feng, T. C. Scott, and A. J. Pearlstein, "Steady Axisymmetric Motion of a Deformable Drops Falling or Rising through a Homoviscous Fluid in a Tube at Intermediate Reynolds Number," J. Fluid Mech. **336**, 1 (1997).

[38] M. J. Fritts, D. E. Fyre, and E. S. Oran, "Numerical Simulations of Fuel Droplet Flows Using a Lagrangian Triangular Mesh," NASA CR-168263 (1983).

[39] P. Y. Liang, T. W. Eastes, and A. Gharakhari, "Computer Simulations of Drop Deformation and Drop Breakup" Proc. 24th. AIAA/ASME/SAE/ASEE Joint Propulsion Conference, Boston, Massachusetts, AIAA-88-3142 (1988).

[40] Z. T. Deng and S. M. Jeng, "Numerical Simulation of Droplet Formation in Convective Flows," AIAA Journal **30**, 1290 (1992).

[41] Z. T. Deng, G. S. Liaw, and L. Chou, "Modeling of Non-Spherical Droplet Dynamics," Proc. 11th. Workshop for Computational Fluid Dynamic Applications in Rocket Propulsion, Huntsville, Alabama, NASA Conference Publication 3221 (1993).

[42] S. P. Seung, C. P. Chen, and Y. S. Chen, "Development of an Atomization Methodology for Spray Combustion," Proc. 11th. Workshop for Computational Fluid Dynamic Applications in Rocket Propulsion, Huntsville, Alabama, NASA Conference Publication 3221 (1993).

[43] S. Zaleski, J. Li, and S. Succi, "Two-Dimensional Navier-Stokes Simulation of Deformation and Breakup of Liquid Patches," Phys. Rev. Lett. **75**, 244 (1995).

[44] S. O. Unverdi and G. Tryggvason, "A Front-Tracking Method for Viscous, Incompressible, Multi-Fluid Flows," J. Comput. Phys. **100**, 25 (1992).

[45] F. H. Harlow and J. E. Welch, "Numerical Calculation of Time-Dependent Viscous Incompressible Flow of Fluid with Free Surface," Phys. Fluids **8**, 2182 (1965).

[46] G. Tryggvason, B. Bunner, O. Ebrat, and W. Tauber, "Computations of Multiphase Flows by

a Finite Difference/Front Tracking Method – I. Multi-Fluid Flows," 29th. Computational Fluid Dynamics, von Karman Institute for Fluid Dynamics Lecture Series 1998-03 (1998).

[47] G. Tryggvason, "Numerical Simulations of the Rayleigh-Taylor Instability," J. Comput. Phys. **75**, 253 (1988).

[48] W. J. A. Dahm, C. M. Scheil, and G. Tryggvason, "Dynamics of Vortex Interaction with a Density Interface," J. Fluid Mech. **205**, 1 (1989).

[49] T. Wairegi and J. R. Grace, "The Behaviour of Large Drops in Immiscible Liquids," Int. J. Multiphase Flow **3**, 67 (1976).

[50] W. J. A. Dahm, C. E. Frieler, and G. Tryggvason, "Vortex Structure and Dynamics in the Near Field of a Coaxial Jet," J. Fluid Mech. **241**, 371 (1992).

[51] G. R. Baker and D. W. Moore, "The Rise and Distortion of a Two-dimensional Gas Bubble in an Inviscid Liquid," Phys. Fluids A **1**, 1451 (1989).

[52] J. B. Heywood, *Internal Combustion Engine Fundamentals* (McGraw-Hill, 1988), p. 522.